machines

MDPI

Article

Nonlinear Dynamics and Combination Resonance of a Flexible Turbine Blade with Contact and Friction of Shrouds

Hua Li [1], Gaofei Yuan [2], Zifeng Yu [1], Yuefang Wang [3,4,*] and Dzianis Marmysh [5]

[1] China Oil & Gas Pipeline Network Corporation, Beijing 100020, China; lihua07@pipechina.com.cn (H.L.)
[2] National Key Laboratory of Helicopter Aeromechanics, China Helicopter Research and Development Institute, Jingdezhen 333001, China; ygf@mail.dlut.edu.cn
[3] Department of Engineering Mechanics, Dalian University of Technology, Dalian 116024, China
[4] State Key Laboratory of Structural Analysis, Optimization and CAE Software for Industrial Equipment, Dalian 116023, China
[5] Department of Theoretical and Applied Mechanics, Belarus State University, 220030 Minsk, Belarus; marmyshde@bsu.by
* Correspondence: yfwang@dlut.edu.cn

Abstract: Flexible shrouded blades are commonly adopted in the last stages of steam turbines where complicated dynamical behavior can be induced by dry friction force generated on contacting interfaces between adjacent shrouds and the geometric nonlinearity due to the structural flexibility of the blades. In this paper, combination resonance caused by contact and friction forces generated on shroud interfaces is investigated, which is a concurrence of 1:3 internal resonance involving the first and second modes in the flapwise direction and the primary resonance of the first flapwise mode. The stiffness and damping at the contact interface are obtained by linearizing the contact and friction forces between shrouds through the harmonic balance method. The vibrating blade is modeled as a beam with a concentrated mass of which the responses under the combination resonance are solved through the multiple-scale method. Sensitivities of response with respect to the angle of shrouds, contact stiffness and rotation speed are illustrated, and the influences of these parameters on the periodicity and amplitudes of steady responses are demonstrated. The parametric regions where the combination resonance occurs are pointed out. Finally, parametric analyses are presented to show how the amplitude–frequency relation of the multiple-scale solutions under the combination resonance vary with detuning and design parameters. The present research provides a designing basis for improving the dynamic performance of flexible shrouded blades and suppressing vibrations of blades by adjusting structural parameters in practical engineering.

Keywords: flexible shrouded blade; combination resonance; contact and friction; harmonic balance method; method of multiple scales

Citation: Li, H.; Yuan, G.; Yu, Z.; Wang, Y.; Marmysh, D. Nonlinear Dynamics and Combination Resonance of a Flexible Turbine Blade with Contact and Friction of Shrouds. *Machines* **2024**, *12*, 59. https://doi.org/10.3390/machines12010059

Academic Editor: Jing Liu

Received: 18 November 2023
Revised: 7 January 2024
Accepted: 8 January 2024
Published: 12 January 2024

1. Introduction

Shrouds have been widely used by developers of multi-stage steam turbines to dissipate vibratory energy and reduce the stress of rotating bladed blisks for the purpose of improving their structural reliability [1]. To ensure the constant flow rate of the steam, the blades mounted on the last-stage blisk are generally designed to be the longest with considerable structural flexibility, which causes an effect of geometric nonlinearity that cannot be ignored. On the other hand, there exists contact and dry friction on the contacting interfaces between adjacent shrouds, which intensifies the nonlinear characteristics as far as the dynamic of the shrouded blades is concerned.

Various studies were published previously devoted to modeling the shrouded blade of turbines, covering the topics of modeling of blades as well as the contact force between adjacent shrouds. Single-blade modeling was adopted to understand the dynamical properties of flexible turbine blades [2,3]. In some publications, the interaction between the reference

blade and the adjacent blades [4–6] was considered, while a few studies were aimed at the vibration of the whole blade disk [7]. Zhou et al. [8] investigated the transverse vibration of composite blades of a wind turbine using a generalized Timoshenko beam. Slender blades that resembled the beam model and a rigid disk were integrated into a continuous model by Shadmani [9] in modal analysis of a turbine blisk. As for the contacts between adjacent shrouds, various models were published for evaluating the inter-shroud action of friction and contact. The effects of macro- and micro-slip between the neighboring blades were established by Griffin [10] and later publications such as [11,12]. Later, Yang and Menq established a special model to predict the resonance of structural response possessing a three-dimensional frictional constraint [13]. Nan et al. [14] translated the contact and friction that acted on the shroud interfaces into an equivalent stiffness as well as damping by means of the harmonic balance method.

In essence, the contact between the shrouds is physically nonlinear and has been regularly simplified as a piecewise linear function of the blade motion. In the view of dynamics, such contact force is attributable to complicated behaviors, e.g., self-excited vibrations, bifurcation of motion, chaos and switch of stability [15]. He et al. [16] proposed a full set of blades subjected to friction and impact forces due to shroud contacting and demonstrated various types of periodic, quasi-periodic and even chaotic motions of the blades. He et al. [17] studied the interaction of bending and torsional vibration of blades, considering the rub and impact between shrouds. As for the nonlinear dynamics of full blisks, achievements were made in mistuned disks, nonlinear resonance frequencies and localization phenomena [18–23].

For the combination resonance of the turbine blade, most of the existing research attended to the internal resonance [24–26], primary resonance [27,28] or combination resonance with both internal and sub- or super-harmonic responses [29–31]. A few publications were dedicated to the combination resonance consisting of the internal and primary resonances of the flexible turbine blade. Li et al. [32] investigated the nonlinear vibration of a blade simultaneously undergoing two resonances (i.e., internal as well as primary), considering aerodynamic force, damping and structural nonlinearity. Yuan and Wang studied internal resonance, primary resonance and the combined multiple modal resonances of a blade [33], where they demonstrated the contribution of primary and internal resonances to the combination resonance in terms of frequencies and energy. It is worth pointing out that, despite the existent works on the nonlinear vibrations of bladed blisks, the combination resonance induced by contact and friction between neighboring blades has yet to be thoroughly understood. Such understanding will provide a better understanding of the dynamical behaviors of flexible shrouded blades and how shroud design influences the blade vibration under the situation of combination resonance.

In the present study, the dynamics of a flexible blade mounted with a shroud are investigated, focusing particularly on the combination resonance of blade vibration that is induced by the contact as well as friction forces applied on the shroud. Firstly, the equivalent stiffness and damping of the shroud due to the normal contact as well as the friction are obtained through the method of harmonic balance, and the blade is simplified as one single continuous beam attached by a concentrated mass. A steady response under the combination resonance is presented through the multiple-scale method. Afterward, influences of design parameters on periodicities and amplitudes are demonstrated for the steady responses. Jumping of amplitude due to the primary resonance and the transfer of vibration energy between resonance modes excited by the internal resonance are pointed out. Finally, amplitude–frequency curves of the multiple-scale solutions under the combination resonance are derived. Parametric analyses are presented to show the effect of detuning and key design parameters on the first and second flapwise modes.

2. Governing Equations of Flexible Shrouded Blade

Figure 1 depicts the sketch of a perfectly tuned, rotating shrouded disk that is commonly used in steam turbines. For such a blisk, all of the shrouded blades are mounted

circumferentially and separated in equal space [34]. Hence, the blisk can be considered to have a cyclic symmetry. In addition, the blades of the final stage of the turbine generally have a large span size to ensure the constant flow rate of the working medium, which will enhance the flexibility of the blade.

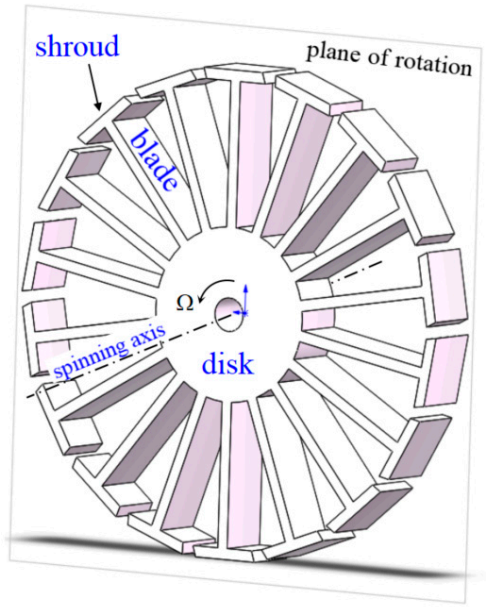

Figure 1. Mechanical model of shrouded rotating disk.

To focus on the overall dynamics of the blade, a macro-slip model is adopted in the present work. The dimension of the shroud mounted at the tip of the blade is small compared with the blade length and is generally rigid as opposed to the long and flexible blade, which can be further treated as a single mass point. The normal contact force between the adjacent shrouds is modeled by a linear spring [16]. Accordingly, the flexible shrouded blade is modeled as a beam with an attached mass that is placed at the tip of the blade, as shown in Figure 2. A Cartesian frame can be set up for the blade with the origin placed at the center of gravity of the root and three axes of x (axial direction), y (flapwise direction) and z (edgewise direction). α represents the tilting angle of the shroud, and Ω is the rotation speed. L is the length of the blade. k_s and δ_s are contact (normal) stiffness and the circumferential gap between shrouds, respectively.

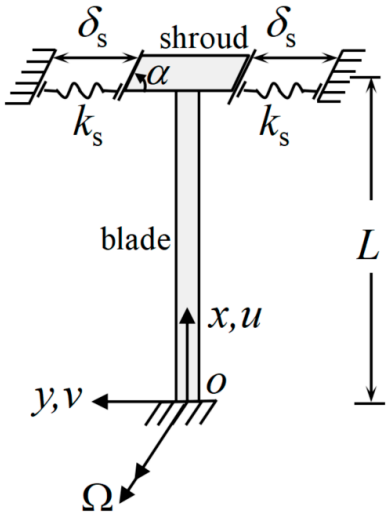

Figure 2. Sketch of a flexible shrouded blade.

2.1. Dynamic Model of Contact between Adjacent Shrouds

Prior to deriving the governing equation of the blade motion, it is necessary to describe the contact action between adjacent shrouds, which is a contribution to the nonlinear dynamics and combination resonance. Hereafter, the equivalent stiffness and damping of the normal and friction between adjacent shrouds are established through the method of harmonic balance.

In this research, the contact force is presumed to change as a piecewise linear function of the relative displacement of two adjacent shrouds, whereas friction carries typical nonlinear characteristics. The states of contact (e.g., separation, stick or slip) depend upon relative displacements in both normal and tangential directions.

In Figure 3, the non-conservative forces on the shroud are aerodynamic force (Q), normal contact force (N_s) and friction (F_s), where

$$Q = Q_0 \sin(l\Omega t), \tag{1}$$

with Q_0 being the amplitude and l the number of guided vanes of the upstream inlet [27].

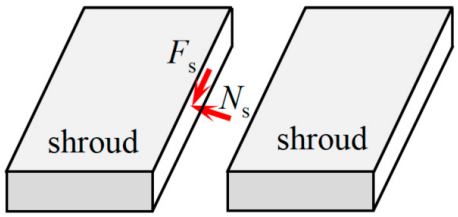

Figure 3. The sketch of aerodynamic, normal and friction forces of the shroud.

The flapwise displacement of the blade, v, can be assumed as [14]

$$v = B\cos(l\Omega t - \phi) = B\cos\vartheta, \tag{2}$$

where B and ϕ stand for the amplitude and phase angle of displacement v, respectively. Then, the contact force between two adjacent shrouds is modeled as

$$N_s = \begin{cases} -k_s(v-\delta_s)\sin\alpha, & v > \delta_s \\ 0, & -\delta_s \le v \le \delta_s \\ -k_s(v+\delta_s)\sin\alpha & v < -\delta_s \end{cases} \tag{3}$$

As for the friction force between two neighboring shrouds, there are two possible situations during one cycle of the vibration based on the change in the normal force when the macro-slip model is adopted: (1) N_s is not zero and time varies during shroud contacting, and (2) N_s is zero when two shrouds separate. The hysteretic loop of the friction force F_s changes along with the tangential relative displacement are depicted in Figure 4. Different from the hysteretic loop of the friction in [14], the influence of the normal force on sliding friction is considered in this paper.

As depicted in Figure 4, the friction force between shrouds starts from point A ($\vartheta = 0$) and changes clockwisely according to the hysteresis loop. Section AB corresponds to the phase of static friction. Then, from point B ($\vartheta = \vartheta_1$) to point C ($\vartheta = \vartheta_2$), the blade begins to slide towards the opposite direction. The segment of BC corresponds to the phase of sliding friction. The separation of adjacent shrouds takes place at point C, and the friction declines to zero at D ($\vartheta = \vartheta_2$). Subsequently, v_t continues to decrease, and the state of friction moves from D to D' ($\vartheta = \pi - \vartheta_2$) where the blade starts to contact the blade from the other side. Section $D'E'$ also corresponds to the phase of static friction, where the blade begins to slide at point E' ($\vartheta = \vartheta_3$). After that, the negative v_t reaches the maximum at A' ($\vartheta = \pi$). Notably, the section $A'A$ in the loop is symmetric with section AA'.

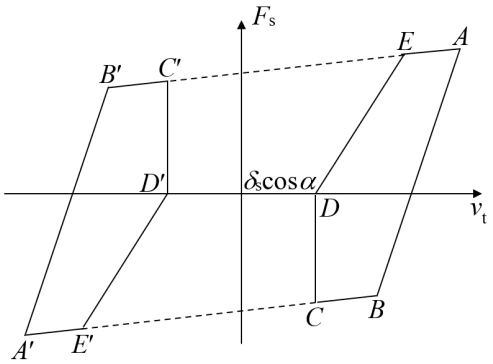

Figure 4. Hysteretic loop of friction versus tangential relative displacement.

Based on the aforementioned hysteretic behavior, the friction force can be modeled in terms of the state of contact between adjacent blades:

$$F_s = \begin{cases} k_t(v_t - B\cos\alpha) + \mu k_s(v - \delta_s)\sin\alpha, & 0 \le \vartheta < \vartheta_1, \quad (A-B) \\ -\mu k_s(v - \delta_s)\sin\alpha, & \vartheta_1 \le \vartheta < \vartheta_2, \quad (B-C) \\ 0, & \vartheta_2 \le \vartheta < \pi - \vartheta_2, \quad (D-D') \\ k_t(v_t + \delta_s\cos\alpha), & \pi - \vartheta_2 \le \vartheta < \vartheta_3, \quad (D'-E') \\ -\mu k_s(v + \delta_s)\sin\alpha, & \vartheta_3 \le \vartheta < \pi, \quad (E'-A') \\ k_t(v_t + B\cos\alpha) + \mu k_s(v + \delta_s)\sin\alpha, & \pi \le \vartheta < \pi + \vartheta_1, \quad (A'-B') \\ \mu k_s(v + \delta_s)\sin\alpha, & \pi + \vartheta_1 \le \vartheta < \pi + \vartheta_2, \quad (B'-C') \\ 0, & \pi + \vartheta_2 \le \vartheta < 2\pi - \vartheta_2, \quad (D'-D) \\ k_t(v_t - \delta_s\cos\alpha), & 2\pi - \vartheta_2 \le \vartheta < \pi + \vartheta_3, \quad (D-E) \\ \mu k_s(v - \delta_s)\sin\alpha, & \pi + \vartheta_3 \le \vartheta < 2\pi, \quad (E-A) \end{cases} \tag{4}$$

where k_t and μ are shear stiffness and the friction coefficient of the contact surface of the shroud. ϑ_1, ϑ_2 and ϑ_3 are the phase angles of the friction force, defined as

$$k_t = \frac{2k_s(1-\nu)}{2-\nu} \tag{5}$$

$$\vartheta_1 = \cos^{-1}\left(\frac{k_t B + 2\mu k_s \delta_s \tan\alpha}{k_t B + 2\mu k_s B \tan\alpha}\right), \vartheta_2 = \cos^{-1}\left(\frac{\delta_s}{B}\right), \ \vartheta_3 = \cos^{-1}\left(-\frac{k_t\delta_s + \mu k_s \delta_s \tan\alpha}{k_t B + \mu k_s B \tan\alpha}\right) \tag{6}$$

To facilitate the dynamical analysis in the present study, the method of harmonic balance (HBM) [35] is used to simplify contact (normal) and friction forces to obtain the stiffness and damping at the shroud surface. For this purpose, one linearizes N_s as

$$N_s = N_{ks}\cos\vartheta + N_{cs}\sin\vartheta = k_n v + c_n\frac{dv}{dt}, \tag{7}$$

where

$$k_n = -\frac{k_s\sin\alpha}{B\pi}(2B\vartheta_2 + B\sin 2\vartheta_2 - 4\delta_s\sin\vartheta_2). \tag{8}$$

Based on Equation (3), the contribution of the blade velocity to the contact force is negligible; hence, one assumes

$$c_n = 0 \tag{9}$$

The friction force between adjacent shrouds can be expressed as

$$F_s = F_{ks}\cos\vartheta + F_{cs}\sin\vartheta = k_f v + c_f\frac{dv}{dt}, \tag{10}$$

where k_f and c_f represent the stiffness and damping of F_s, respectively.

$$k_f = \frac{1}{B\pi}\begin{pmatrix} k_t B\cos\alpha\left[(\vartheta_3+\vartheta_2+\vartheta_1-\pi)+\frac{(\sin 2\vartheta_3+\sin 2\vartheta_2+\sin 2\vartheta_1)}{2}-2\sin\vartheta_1\right] \\ +2k_t\delta_s\cos\alpha(\sin\vartheta_3-\sin\vartheta_2)+\mu k_s B\sin\alpha\left(\vartheta_1+\frac{B\sin 2\vartheta_1}{2}\right)-2\mu k_s\delta_s\sin\alpha\sin\vartheta_1 \end{pmatrix} \tag{11}$$

$$c_f = \frac{1}{-l\Omega B\pi}\begin{pmatrix} 2k_t B\cos\alpha\left[(\cos\vartheta_1-1)+\frac{1-\cos 2\vartheta_1+\cos 2\vartheta_2-\cos 2\vartheta_3}{4}\right] \\ -2k_t\delta_s\cos\alpha(\cos\vartheta_3+\cos\vartheta_2) \\ +2\mu k_s\delta_s\sin\alpha(\cos\vartheta_1-\cos\vartheta_3-1)-\mu k_s B\sin\alpha\frac{\cos 2\vartheta_1-1}{2} \end{pmatrix} \tag{12}$$

2.2. Governing Equations of Blade Vibration

The blade in the present study is modeled as a beam attached by a concentrated shroud mass at the tip of the blade. For blades carrying small installation angles, their torsional rigidities are sufficient; hence, the twisting movement of the rotating blade can be effectively neglected. Thus, the edgewise deformation of the blade caused by the torsion should be neglected. Additionally, the dynamic spanwise (axial) displacement can be described as minor as opposed to the pre-stretching caused by centrifugal load on the blade [32]. Therefore, the interaction between the flapwise and axial motions is fulfilled by means of the centrifugal stiffening upon lateral vibration frequencies. Based on Figure 2, the equation of the blade flapwise vibration is established, which reads

$$\begin{aligned}[m_l+m_s\delta(x-L)]\ddot{v}+c_v\dot{v}-[m_l v+m_s\delta(x-L)]\Omega^2 v+(EIv'')''-(EAu'v')' \\ -\left(\tfrac{1}{2}EAv'^3\right)'=(-Q+N_s\sin\alpha+F_s\cos\alpha)\delta(x-L),\end{aligned} \tag{13}$$

where $v = v(x,t)$ is the dynamic displacement of the blade in the flapwise. $u = u(x)$ is the spanwise (axial) displacement generated by centrifugal force of the blade. The EI and EA are bending and tensile stiffnesses of the blade, respectively. m_l represents the linear mass density of the blade. m_s is the mass of shroud. The term EAv'^3 is the outcome of geometric nonlinearity due to the structural flexibility of the blade, and δ is the Dirac function of x. The overhead dot and prime represent the partial derivatives of a physical quantity with respect to time t and x, respectively, i.e.,

$$\dot{(\cdot)} \stackrel{\text{def}}{=} \partial(\cdot)/\partial t, \text{ and } (\cdot)' \stackrel{\text{def}}{=} \partial(\cdot)/\partial x \tag{14}$$

Subsequently, the flapwise displacement of the blade is decomposed in the modal space

$$v(x,t) = \sum_k \gamma_k(x) q_k(t), \tag{15}$$

where γ_k stands for the mode shape of order k of the beam under given boundary conditions in the flapwise direction, and q_k are the generalized (modal) coordinates of γ_k. Thus, Equation (13) can be simplified using the Galerkin method considering the first- and second-order modal coordinates, as

$$\ddot{q}_k + c_k\dot{q}_k + \omega_k^2 q_k + g_{k,1}q_1^3 + 3g_{k,2}q_1^2 q_2 + 3g_{k,3}q_1 q_2^2 + g_{k,4}q_2^3 = f_k\sin(l\Omega t), \quad k = 1,2, \tag{16}$$

where c_k, ω_k, $g_{k,j}$ and f_k are defined in Equations (A1)–(A8), Appendix A. Further, Equation (16) can be rewritten with the introductions of non-dimensional notations:

$$\bar{q}_i = \frac{q_i}{\delta_s} \text{ and } \tau = \Omega t, \tag{17}$$

such that one has the compact governing equations

$$\ddot{\bar{q}}_k + \bar{c}_{k,k}\dot{\bar{q}}_k + \bar{\omega}_{k,k}^2\bar{q}_k + \bar{g}_{k,1}\bar{q}_1^3 + 3\bar{g}_{k,2}\bar{q}_1^2\bar{q}_2 + 3\bar{g}_{k,3}\bar{q}_1\bar{q}_2^2 + \bar{g}_{k,4}\bar{q}_2^3 = \bar{f}_k\sin(l\tau), \quad k = 1,2, \tag{18}$$

where $\bar{c}_k$, $\bar{\omega}_k$, $\bar{g}_{k,j}$ and $\bar{f}_k$ are defined in Equations (A9)–(A15), Appendix A.

3. Multiple-Scale Solutions under Combination Resonance

The multiple-scale method will be adopted in this section for solving Equation (18). To construct the analytical solution of the problem, a small, artificial bookkeeping parameter is introduced to order the quantities of dynamic displacements, damping and aerodynamic forces before they are inserted into Equation (18). Thus, one has

$$\overline{q}_k = \varepsilon\widetilde{q}_k, \overline{c}_{k,k} = \varepsilon\widetilde{c}_{k,k}, \overline{f}_k = \varepsilon^3\widetilde{f}_k, k = 1,2 \tag{19}$$

Herein, the regular scale of time is replaced with three temporal scales, i.e.,

$$T_0 = t, T_1 = \varepsilon t, T_2 = \varepsilon^2 t \tag{20}$$

Then, $\widetilde{q}_k$ is expanded using the power series of ε and the new scales

$$\widetilde{q}_k = \sum_{j=0}^{2} \varepsilon^j \widetilde{q}_{k,j}(T_0, T_1, T_2), \quad k = 1,2 \tag{21}$$

Let $D_j = \partial(\cdot)/\partial T_j$ and substitute Equations (19) and (21) back to Equation (18), then equate their same orders of ε. In doing so, one obtains

$$\text{order } \varepsilon \; D_0^2\widetilde{q}_{k,0} + \overline{\omega}_k^2\widetilde{q}_{k,0} = 0 \tag{22}$$

$$\text{order } \varepsilon^2 \; D_0^2\widetilde{q}_{k,1} + \overline{\omega}_k^2\widetilde{q}_{k,1} = -2D_0D_1\widetilde{q}_{k,0} - \widetilde{c}_{k,k}D_0\widetilde{q}_{k,0} \tag{23}$$

$$\text{order } \varepsilon^3 \; D_0^2\widetilde{q}_{k,2} + \overline{\omega}_k^2\widetilde{q}_{k,2} = F_k\left(\widetilde{q}_{j,0}, \widetilde{q}_{j,1}, l\right), \tag{24}$$

where $k, j = 1,2$.

For Equation (22), let us assume that

$$\widetilde{q}_{k,0} = A_k e^{i\overline{\omega}_k T_0} + complex\ conjugate, \quad k = 1,2 \tag{25}$$

and then substitute these back to Equation (23) to obtain

$$2D_1A_k + \widetilde{c}_{k,k}A_k = 0, \quad k = 1,2, \tag{26}$$

which further leads to

$$\widetilde{q}_{k,1} = A_k e^{i\overline{\omega}_k T_0} + complex\ conjugate, \quad k = 1,2 \tag{27}$$

The highest $\widetilde{q}_k$ can be evaluated through the perpetual term of Equation (24).

A particular type of combination resonance is of present interest, i.e., when a particular internal resonance takes places with $\overline{\omega}_2 = 3\overline{\omega}_1$ ("1:3"). To be specific, the frequencies of the first-order flap mode are triple the second-order flapwise frequency, and alongside, there is a primary resonance of the first flapwise mode (i.e., $\overline{\omega}_1 = l$). Under this situation, one can assume that $\varepsilon A_k = 1/2\alpha_k e^{i\beta_k}$. By introducing new phases $\gamma_1 = \sigma_1 T_1 - \beta_1$, $\gamma_2 = \beta_2 - 3\beta_1 - \sigma_2 T_1$, one obtains the equations of motion for the amplitudes of εA_k

$$\dot{\alpha}_1 = -\frac{c_{1,1}}{2}\alpha_1 - \frac{3g_{1,2}}{8\overline{\omega}_1}\alpha_1^2\alpha_2 \sin\gamma_2 - \frac{f_1}{2\overline{\omega}_1}\cos\gamma_1 \tag{28}$$

$$\dot{\alpha}_2 = -\frac{c_{2,2}}{2}\alpha_2 + \frac{g_{2,1}}{8\overline{\omega}_2}\alpha_1^3 \sin\gamma_2 \tag{29}$$

and also for the phases of the motion

$$\dot{\gamma}_1 = \left(\varepsilon\sigma_2 + \frac{c_{1,1}^2}{8\overline{\omega}_1}\right) - \frac{3g_{1,1}}{8\overline{\omega}_1}\alpha_1^2 - \frac{3g_{1,3}}{4\overline{\omega}_1}\alpha_2^2 - \frac{3g_{1,2}}{8\overline{\omega}_1}\alpha_1\alpha_2\cos\gamma_2 + \frac{f_1}{2\overline{\omega}_1}\sin\gamma_1 \tag{30}$$

$$\dot{\gamma}_2 = \left(\frac{3c_{1,1}^2}{8\overline{\omega}_1} - \frac{c_{2,2}^2}{8\overline{\omega}_2} - \varepsilon\sigma_1\right) - \left(\frac{9g_{1,1}}{8\overline{\omega}_1} - \frac{3g_{2,2}}{4\overline{\omega}_1}\right)\alpha_1^2 - \left(\frac{9g_{1,3}}{4\overline{\omega}_1} - \frac{9g_{2,4}}{4\overline{\omega}_1}\right)\alpha_2^2 + \frac{3f_1}{2\overline{\omega}_1\alpha_1}\sin\gamma_1 - \left(\frac{9g_{1,2}\alpha_1\alpha_2}{8\overline{\omega}_1} - \frac{g_{2,1}\alpha_1^3}{8\overline{\omega}_1\alpha_2}\right)\cos\gamma_2 \tag{31}$$

The steady solutions for these responses are determined through vanishing the right sides of Equations (28)–(31), which correspond to the fixed-point states of amplitudes of the first and second flapwise modes as well as their phases. The stability of the steady motion can be evaluated in terms of the eigenvalues of the following Jacobian matrix of the fixed points

$$\boldsymbol{J} = \begin{bmatrix} \frac{\partial\dot{\alpha}_1}{\partial\alpha_1} & \frac{\partial\dot{\alpha}_1}{\partial\alpha_2} & \frac{\partial\dot{\alpha}_1}{\partial\dot{\gamma}_1} & \frac{\partial\dot{\alpha}_1}{\partial\dot{\gamma}_2} \\ \frac{\partial\dot{\alpha}_2}{\partial\alpha_1} & \frac{\partial\dot{\alpha}_2}{\partial\alpha_2} & \frac{\partial\dot{\alpha}_2}{\partial\dot{\gamma}_1} & \frac{\partial\dot{\alpha}_2}{\partial\dot{\gamma}_2} \\ \frac{\partial\dot{\gamma}_1}{\partial\alpha_1} & \frac{\partial\dot{\gamma}_1}{\partial\alpha_2} & \frac{\partial\dot{\gamma}_1}{\partial\dot{\gamma}_1} & \frac{\partial\dot{\gamma}_1}{\partial\dot{\gamma}_2} \\ \frac{\partial\dot{\gamma}_2}{\partial\alpha_1} & \frac{\partial\dot{\gamma}_2}{\partial\alpha_2} & \frac{\partial\dot{\gamma}_2}{\partial\dot{\gamma}_1} & \frac{\partial\dot{\gamma}_2}{\partial\dot{\gamma}_2} \end{bmatrix}, \tag{32}$$

where the components of $\boldsymbol{J}$ are provided in Equations (A16)–(A19), Appendix A. The response is said to be asymptotically stable if all of the eigenvalues possess negative real parts.

Afterwards, the approximations of $\overline{q}_1$ and $\overline{q}_2$ can be obtained as

$$\overline{q}_1 = \alpha_1\cos(l\Omega t - \gamma_1) + O\left(\varepsilon^3\right) \tag{33}$$

$$\overline{q}_2 = \alpha_2\cos(3l\Omega t - 3\gamma_1 - \gamma_2) + O\left(\varepsilon^3\right) \tag{34}$$

When the combination resonance happens, the steady responses are determined through conditions

$$\left[\left(\varepsilon\sigma_1 + 3\varepsilon\sigma_2 + \frac{c_{2,2}^2}{8\overline{\omega}_2}\right)\frac{6g_{1,2}}{\overline{\omega}_1}\alpha_2^2 - \left(\varepsilon\sigma_1 + \frac{c_{1,1}^2}{8\overline{\omega}_1}\right)\frac{2g_{2,1}}{\overline{\omega}_2}\alpha_1^2 + \left(\frac{3g_{1,3}g_{2,1}}{2\overline{\omega}_1\overline{\omega}_2} - \frac{9g_{1,2}g_{2,2}}{2\overline{\omega}_1\overline{\omega}_2}\right)\alpha_1^2\alpha_2^2 + \frac{3g_{1,1}g_{2,1}}{4\overline{\omega}_1\overline{\omega}_2}\alpha_1^4 - \frac{9g_{1,2}g_{2,4}}{4\overline{\omega}_1\overline{\omega}_2}\alpha_2^4\right]^2 = \left(\frac{f_1g_{2,1}\alpha_1}{\overline{\omega}_1\overline{\omega}_2}\right)^2 - \left(\frac{g_{2,1}c_{1,1}}{\overline{\omega}_2}\alpha_1^2 + \frac{3g_{1,2}c_{2,2}}{\overline{\omega}_1}\alpha_2^2\right)^2 \tag{35}$$

$$\left(\varepsilon\sigma_1 + 3\varepsilon\sigma_2 + \frac{c_{2,2}^2}{8\overline{\omega}_2} - \frac{2g_{2,2}\alpha_1^2}{4\overline{\omega}_2} - \frac{2g_{2,4}\alpha_2^2}{8\overline{\omega}_2}\right) = \left(\frac{g_{2,1}\alpha_1^3}{8\overline{\omega}_2\alpha_2}\right)^2 - \frac{c_{2,2}^2}{4} \tag{36}$$

Nonetheless, $\alpha_{1,2}$ are constrained by the inequalities

$$\left(\frac{f_1g_{2,1}\alpha_1}{\overline{\omega}_1\overline{\omega}_2}\right)^2 - \left(\frac{f_1g_{2,1}c_{1,1}}{\overline{\omega}_2}\alpha_1^2 + \frac{3g_{1,2}c_{2,2}}{\overline{\omega}_1}\alpha_2^2\right)^2 \geq 0, \left(\frac{g_{2,1}\alpha_1^3}{4\overline{\omega}_2\alpha_2}\right)^2 - \frac{c_{2,2}^2}{4} \geq 0 \tag{37}$$

in order to assure the absolutes of $\sin\gamma_{1,2}$ and $\cos\gamma_{1,2}$ in Equations (28)–(31) are not greater than 1.

In the solution procedure, a simulation is implemented using the Runge–Kutta method with variable step size to obtain numerical results of Equation (18) and the analytical results of the transient system (28)–(31), whereas the analytical steady Equations (35)–(36) are solved through Newton's iteration method. Nevertheless, it is necessary to solve the amplitude of the steady response (i.e., B in Equation (2)) via iterations before the solution of the governing equations begins. Such an iterative process for B is described in Appendix B.

4. Nonlinear Dynamics and Combination Resonance of Shrouded Blade

A flexible shrouded blade is used for examples and discussions. The major parameters involving the blade design and operation are provided in Table 1. The natural frequencies are $\overline{\omega}_1 = 0.7580$ and $\overline{\omega}_2 = 2.9238$ for the first-order and second-order modes in the flapwise

direction. However, these frequencies become $\overline{\omega}_1 = 0.9993$ and $\overline{\omega}_2 = 2.9954$ when one considers the action of contact and friction on the shroud. The condition for concurrence of an internal resonance of type 1:3 between the two flapwise modes and the primary resonance of the first flapwise mode is expected when considering the aforementioned contact and friction.

Table 1. Major parameters of the blade.

Parameter	Value	Parameter	Value
c_v	10 N·s/m	e	0.25 m
EI	5.41×10^4 N·m^2	EA	1.08×10^9 N
k_s	3.55 MN/m	L	1.05 m
m_l	40.13 kg/m	m_s	0.2 kg
Q_0	50	α	60°
δ_s	2.0×10^{-5} m	l	1
μ	0.3	Ω	6900 r/min

To validate the proposed method, the steady responses of the original Equation (18) are solved with the analytical, multiple-scale results $\overline{q}_k$ through Equations (33)–(34), which are obtained by computing Equations (28)–(31). As shown in Figure 5, these analytical solutions are found in good agreement with their numerical counterparts. Their discrepancies are inevitable, since higher order terms have been excluded from multiple-scale-based expansions, and they appear more noticeable for the second flapwise mode than the first. In summary, the proposed modeling and approximate approach are applicable for steady-response solutions of the shrouded blade in the situation of combination resonance.

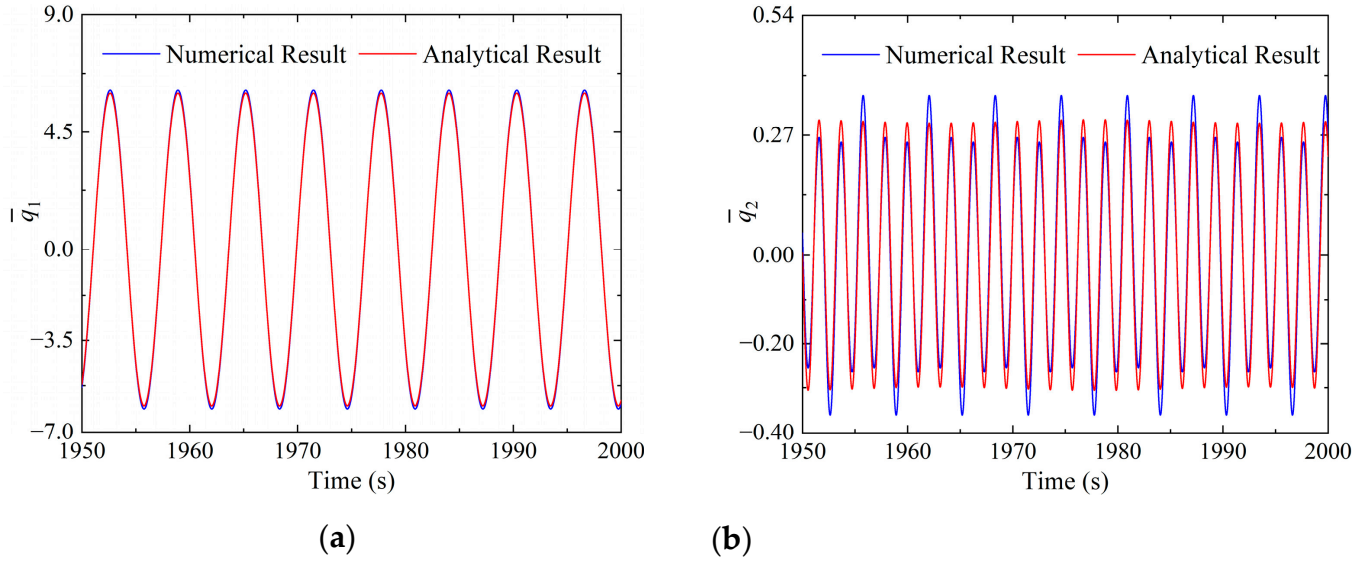

Figure 5. Analytical and numerical steady responses. (**a**) First flapwise mode and (**b**) second flapwise mode.

4.1. Steady Responses of Flexible Shrouded Blade

For flexible blades, the tilting angle and contact stiffness of the shroud are key to the contact status of adjacent shrouds. Further, the blade rotating induces centrifugal load and the subsequent spinning softening that reduces the axial stiffness of the blade. In the following, the original governing Equation (18) is solved with various tilting angle, contact stiffness and rotation speed values to reflect their influence on the response.

4.1.1. Effect of Tilting Shroud

The bifurcation diagram of the blade vibration is demonstrated using the tilting angle of shroud varying between 0 and 90°, Figure 6. Based on the characteristic of the steady

response of the first-order and second-order flapwise modes, the range of the tilting angle is divided into three stages, denoted by stage-I, -II and -III, respectively, with $\alpha_1 = 38.96°$ and $\alpha_2 = 83.65°$ being the dividing points that separate the stages.

The steady responses of the first-order mode $\overline{q}_1$ under variable α are shown in Figure 6a. In stage-I, $\overline{q}_1$ is quasi-periodic motion. Then, $\overline{q}_1$ becomes periodic-1, and the resonance peak of the primary resonance, $\overline{\omega}_1 = l$, can be observed in stage-II. In addition, the jumping of the amplitude and the phenomenon of so-called "hardening" can be seen for stage-II, owing to the geometric nonlinearity originating from Equation (13). Finally, for stage-III, $\overline{q}_1$ is converted back to quasi-periodic motion. It is worthwhile to mention the curving of the resonance summit towards the side where the ratio between the frequency of external excitation and natural frequency, $l/\overline{\omega}_1$, goes up is defined as the hardening spring. In these cases, the jumping of the amplitude and the unstable motion appear in the steady response. However, the steady response is obtained through the Runge–Kutta method in Section 4.1, by which only the stable motion can be observed.

Corresponding to the first flapwise mode, the periodicity of $\overline{q}_2$ is the same as that of $\overline{q}_1$ in stage-I and -III, but $\overline{q}_2$ represents 3-periodic motion in stage-II, Figure 6b. In addition, the jumping of amplitude and the hardening phenomenon caused by the primary resonance can also be observed in stage-II. This is because the primary and internal resonances concur as $\overline{\omega}_1 = l$ and $\overline{\omega}_2 = 3\overline{\omega}_1$, which leads to the desired combination resonance. Therefore, the primary resonance is also observed in $\overline{q}_2$ due to the exchanges in energy between the first-order and second-order modes in the flapwise direction.

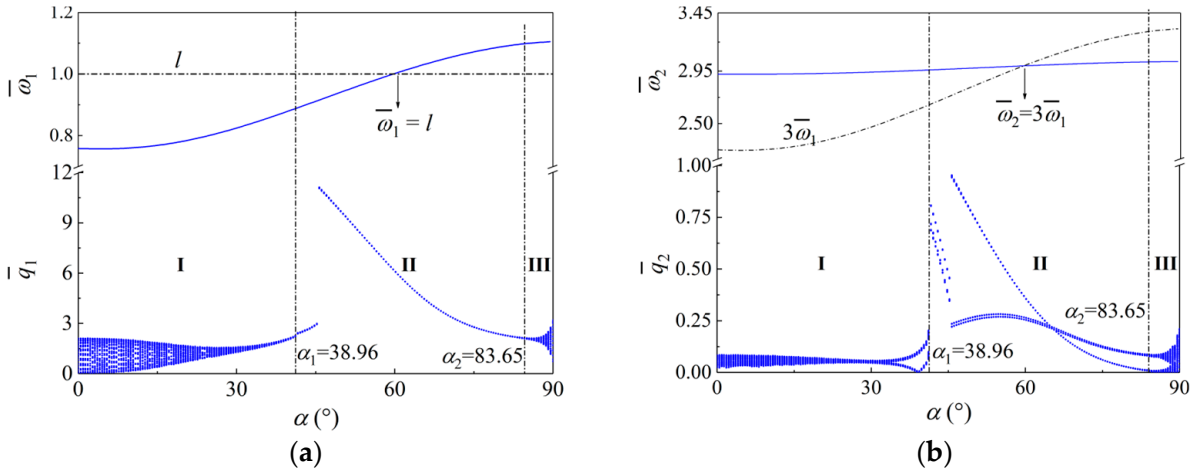

Figure 6. Bifurcation of the blade under variable α. (**a**) $\overline{q}_1$ and (**b**) $\overline{q}_2$.

Further examinations are made focusing on the blade vibration carrying four different tilts angle of shrouds: 4.07° (in stage-I), 40.28°, 40.28° (in stage-II) and 85.48° (in stage-III), and the results are provided through Figures 7–10. As found in Figure 7, both $\overline{q}_1$ and $\overline{q}_2$ are quasi-periodic motions with spectra containing the aerodynamic frequency f_Q, the first flapwise frequency f_{q1} and the combined frequencies of $f_{q1} + 2f_Q$, $2f_{q1} + f_Q$ and $3f_Q$. Further, the amplitude of $\overline{q}_1$ is synchronous and π is out-of-phase against the amplitude of $\overline{q}_2$. This implies that it is likely to have internal resonance when α is small, since the curving of the resonance summit occurs as the blade appears hardened in this scenario. The energy carried by the first order flapwise mode is able to transmit to the second flapwise mode and vice versa.

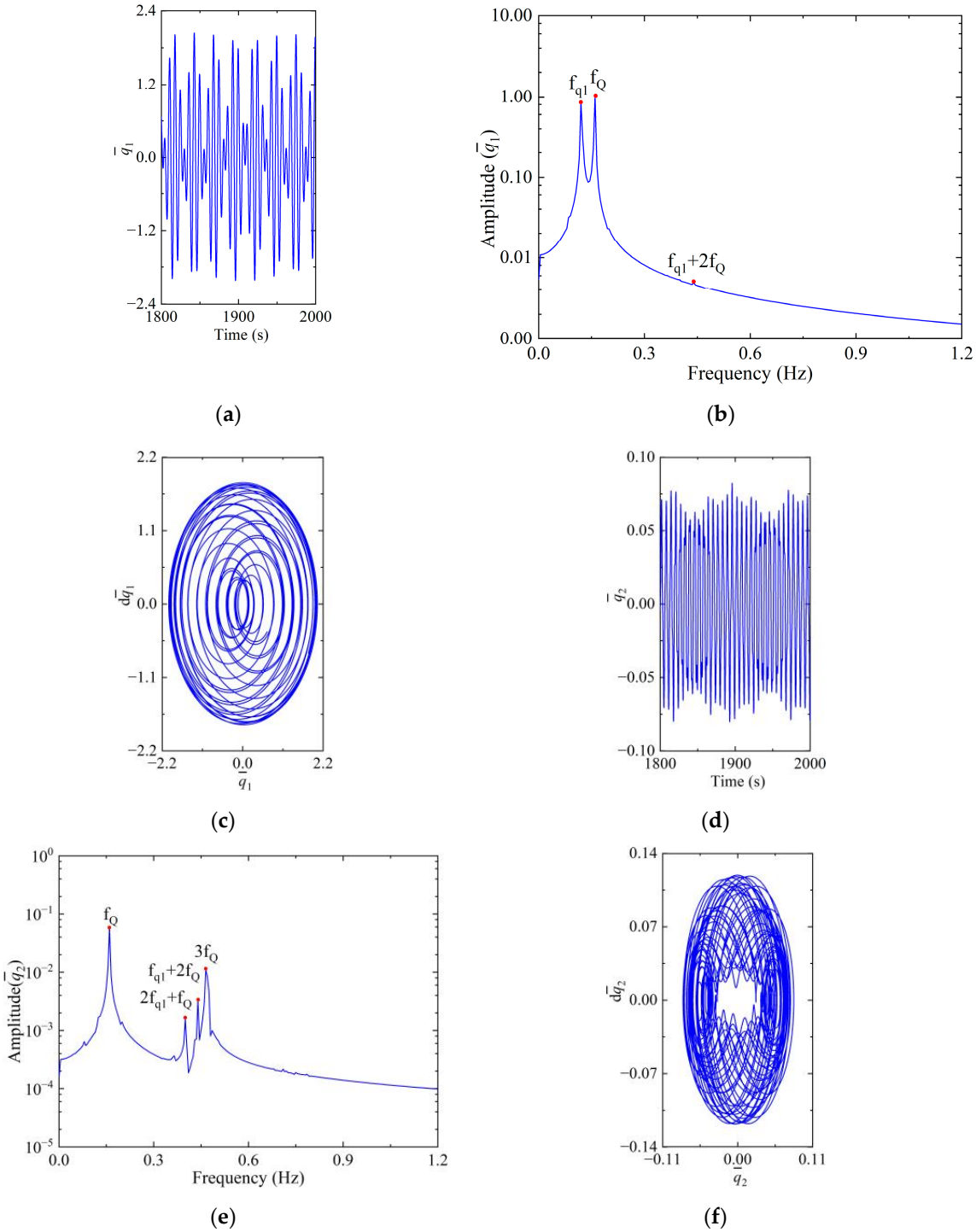

Figure 7. Steady responses of the blade with $\alpha = 4.07°$. (**a**) Time history, (**b**) frequency spectra and (**c**) phase diagram of $\bar{q}_1$; (**d**) time history, (**e**) frequency spectra and (**f**) phase diagram of $\bar{q}_2$.

The steady responses of the blade with $\alpha = 40.28°$ and $44.81°$ are shown in Figures 8 and 9, respectively. $\bar{q}_1$ and $\bar{q}_2$ are identified as periodic-1 motion and periodic-3 motion, respectively, and both $\bar{q}_1$ and $\bar{q}_2$ are governed by f_Q and its odd-fold multiples (i.e., $3f_Q$, $5f_Q$ and so forth). The exchanges in energy between the modes can be observed clearly in Figure 8 but not in Figure 9. This is explained by the fact that the primary resonance is subjected to a strong enhancement on the steady response, which happens when $\alpha = 44.81°$. Although the amplitude increases under primary resonance, the change in motion caused solely by internal resonance is minor and thus can hardly be observed in Figure 9.

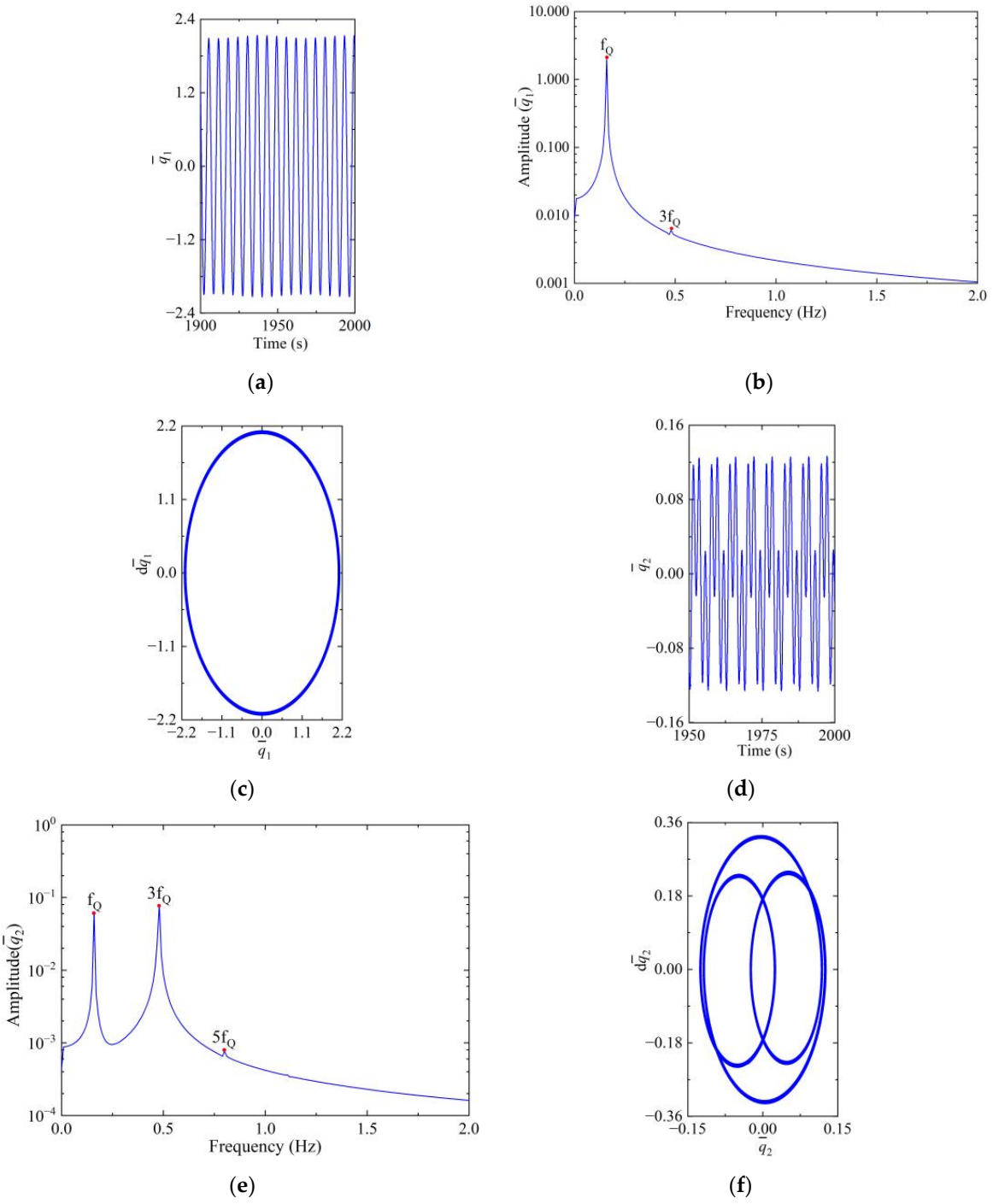

Figure 8. Steady responses of the blade with α = 40.28°. (**a**) Time history, (**b**) frequency spectra and (**c**) phase diagram of $\bar{q}_1$; (**d**) time history, (**e**) frequency spectra and (**f**) phase diagram of $\bar{q}_2$.

The steady response of the blade when $\alpha = 85.48°$ is shown in Figure 10. Both $\bar{q}_1$ and $\bar{q}_2$ are found to be quasi-periodic with dominant spectra of f_Q, the first flapwise frequency f_{q1} and the combined frequencies of $f_{q1} + 2f_Q$, $2f_{q1} + f_Q$ and $3f_Q$. With the current section of α, the aforementioned exchanges in energy between the aforementioned modes cannot be observed. In fact, the frequency difference between these modes grows with the increasing α (c.f. Figure 6b), which weakens the effect of internal resonance on these modes.

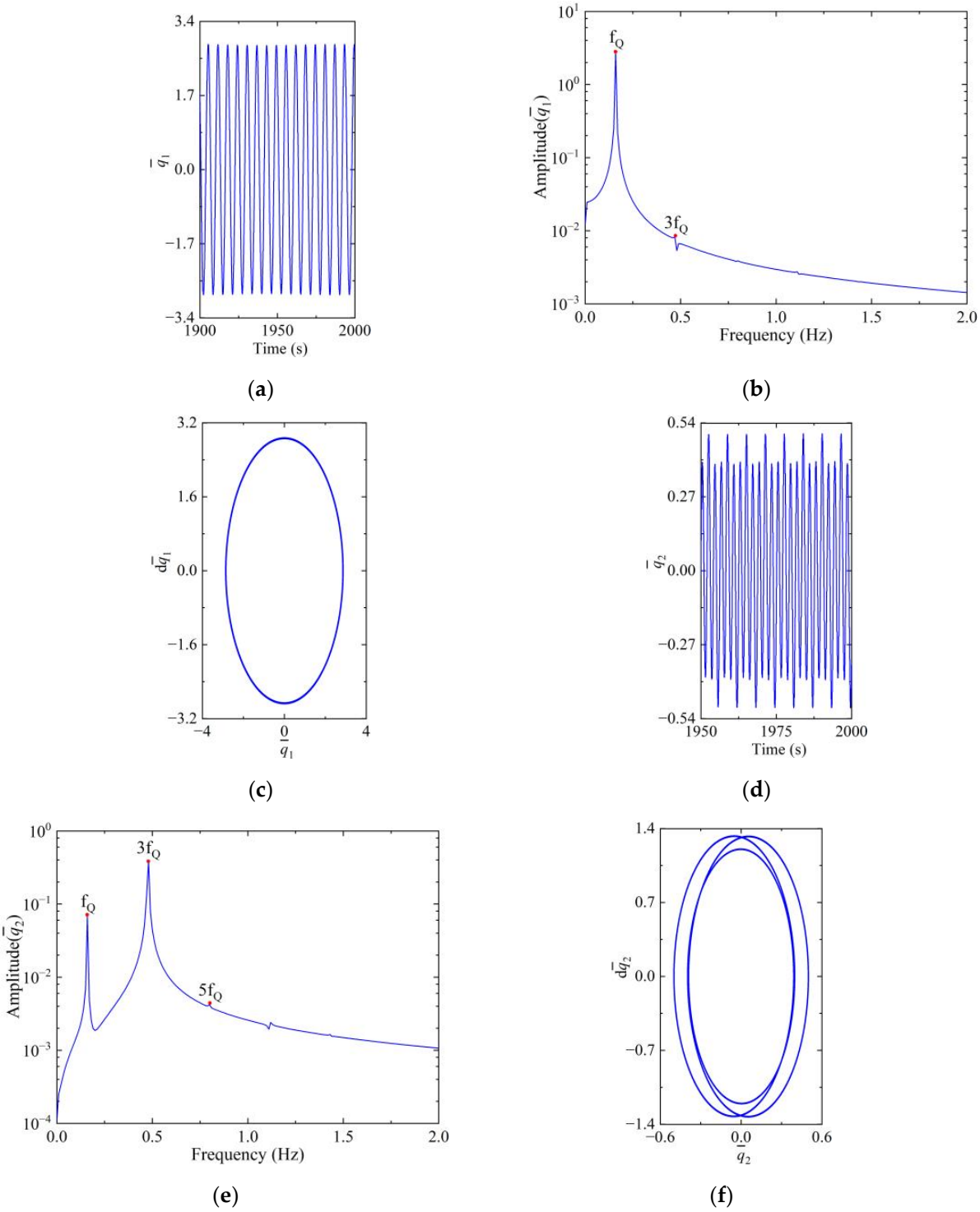

Figure 9. Steady responses of the blade with $\alpha = 44.81°$. (**a**) Time history, (**b**) frequency spectra and (**c**) phase diagram of $\bar{q}_1$; (**d**) time history, (**e**) frequency spectra and (**f**) phase diagram of $\bar{q}_2$.

4.1.2. Effect of Contact Stiffness

In the following, the vibration response of the blade is studied using different stiffness values of normal contact. The bifurcation of the blade vibration is shown in Figure 11, where the contact stiffness ranges from 1 MN/m to 10 MN/m. Similar to Section 4.1.1, the range of k_s is divided into three stages, where $k_{s1} = 1.72$ and $k_{s2} = 6.97$ MN/m are the dividing points of these stages.

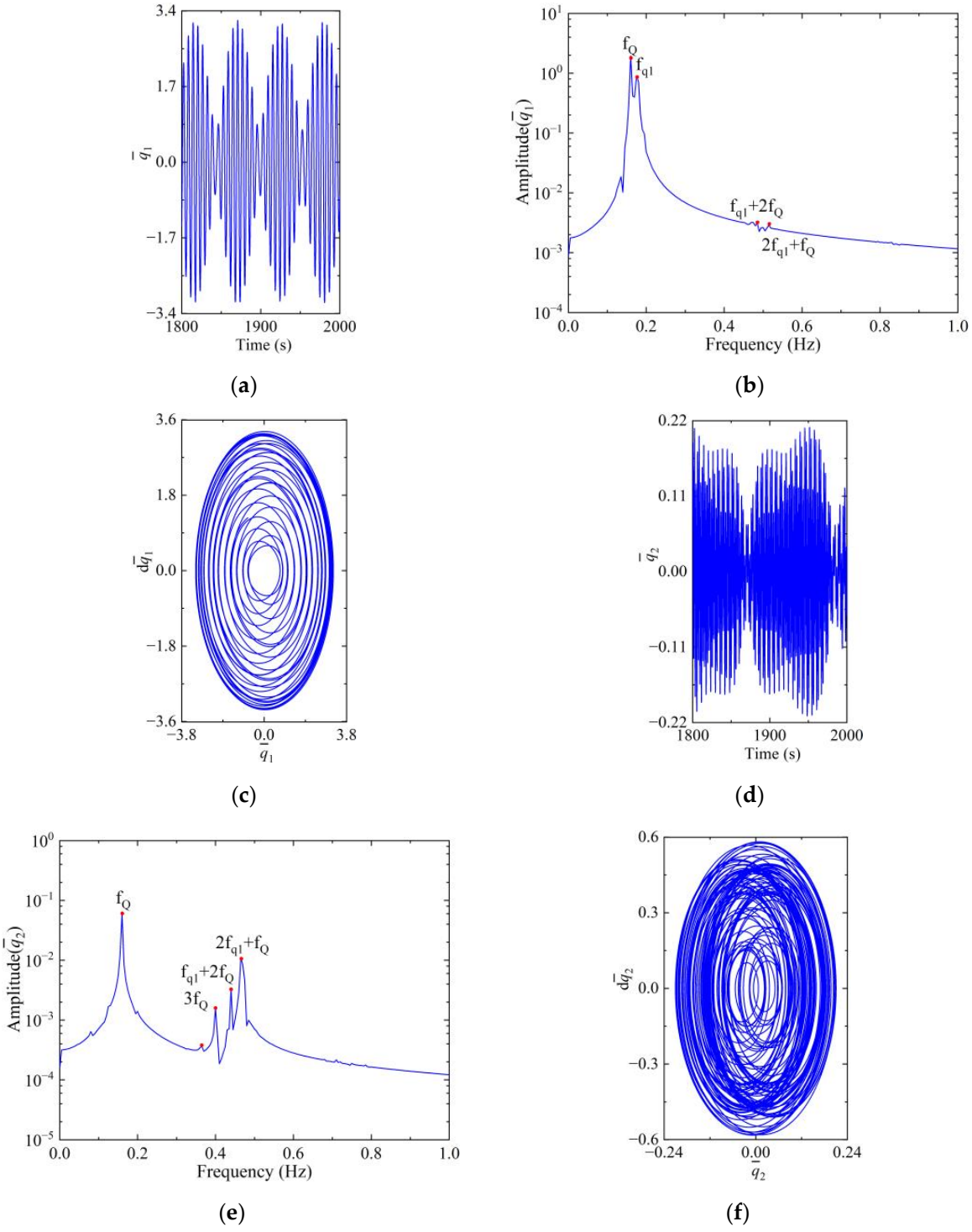

Figure 10. Steady responses of the blade with $\alpha = 85.48°$. (**a**) Time history, (**b**) frequency spectra and (**c**) phase diagram of $\bar{q}_1$; (**d**) time history, (**e**) frequency spectra and (**f**) phase diagram of $\bar{q}_2$.

In Figure 11a, the steady $\bar{q}_1$ is identified as a periodic-1 motion in the entire range of k_s. Again, jumping of amplitude and hardening spring due to the primary resonance can be observed in stage-II. As for the steady second flapwise mode $\bar{q}_2$, it is periodic-1 in stages-I and III but periodic-3 in stage-II, Figure 11b. Moreover, the energy exchanges caused by internal resonance occur in stage-II; thereby, the jumping of the amplitude and the hardening spring due to the primary resonance can also be observed.

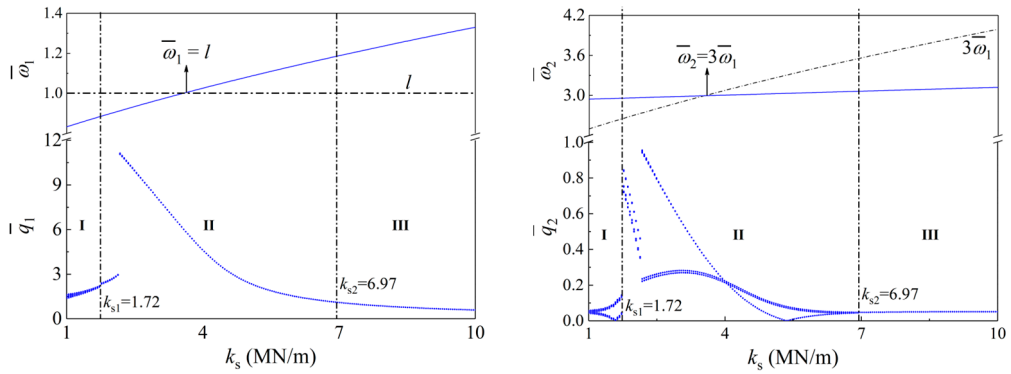

Figure 11. Bifurcation of the blade with variable k_s. (**a**) $\bar{q}_1$ and (**b**) $\bar{q}_2$.

Further explorations are carried out using three different contact stiffness values, i.e., 1.407 MN/m (in stage-I), 2.764 MN/m (in stage-II) and 8.191 MN/m (in stage-III), and the response is provided through Figures 12–14. As depicted in Figure 12, both $\bar{q}_1$ and $\bar{q}_2$ are periodic-1 motions and are spectrally governed by f_Q and its odd multiples ($3f_Q$ and $5f_Q$, etc.). Similar to previous cases, the amplitudes of $\bar{q}_1$ and $\bar{q}_2$ are both periodic, while the amplitude of $\bar{q}_1$ is synchronous and π is out-of-phase against the amplitude of $\bar{q}_2$. Comparing the results presented in the three figures, it is found that the first flapwise modal response is always period-1. Nonetheless, the response of the second flapwise mode changes from a period-1 to period-3 motion and then returns to period-1 when the stiffness of normal contact increases.

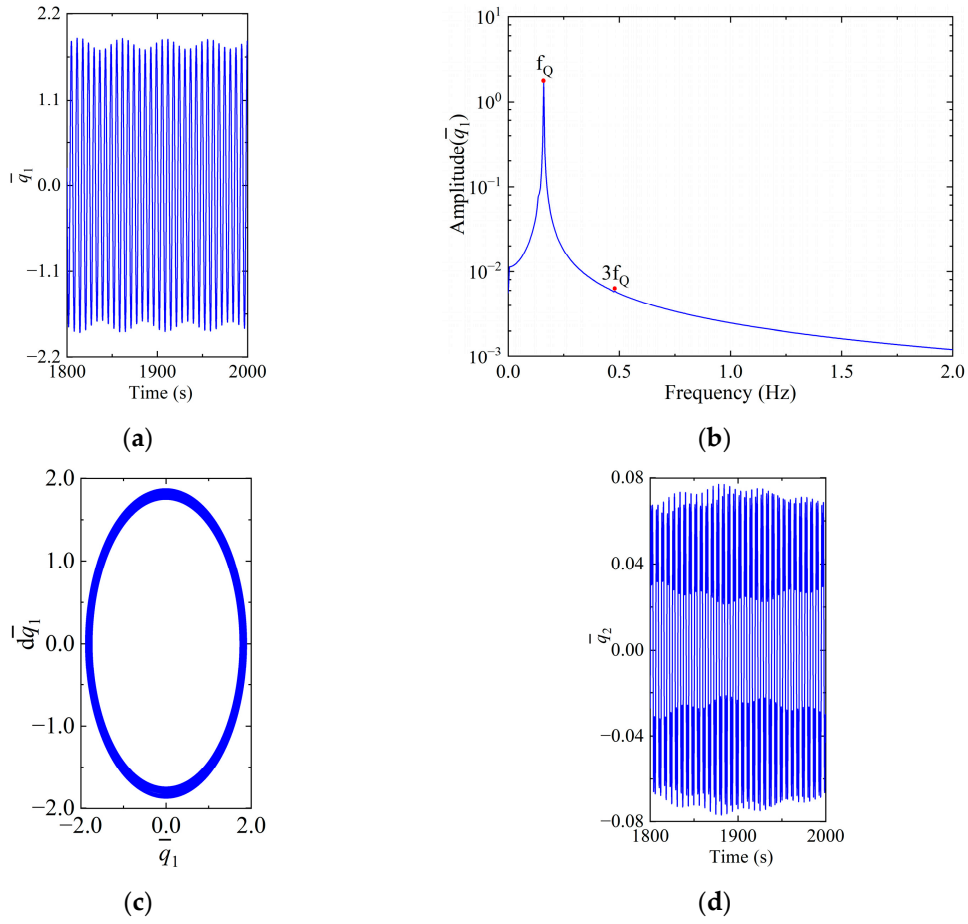

Figure 12. *Cont.*

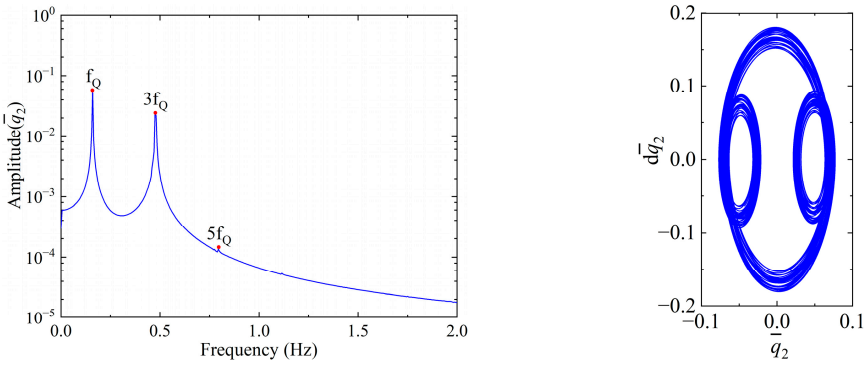

(**e**) (**f**)

Figure 12. Steady responses of the blade with k_s = 1.407 MN/m. (**a**) Time history, (**b**) frequency spectra and (**c**) phase diagram of $\bar{q}_1$; (**d**) time history (**e**) frequency spectra and (**f**) phase diagram of $\bar{q}_2$.

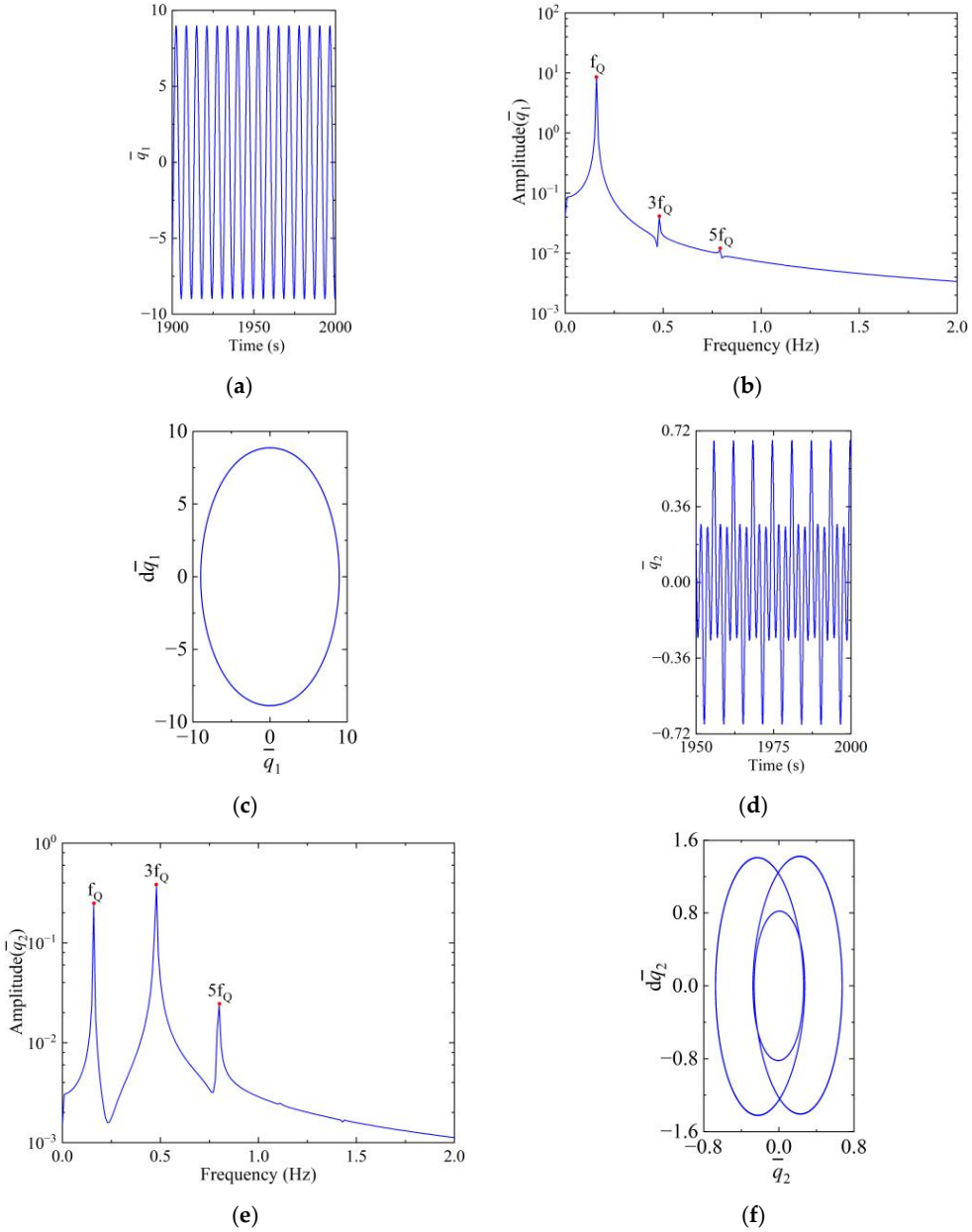

(**a**) (**b**)

(**c**) (**d**)

(**e**) (**f**)

Figure 13. Steady responses of the blade with k_s = 2.764 MN/m. (**a**) Time history, (**b**) frequency spectra and (**c**) phase diagram of $\bar{q}_1$; (**d**) time history, (**e**) frequency spectra and (**f**) phase diagram of $\bar{q}_2$.

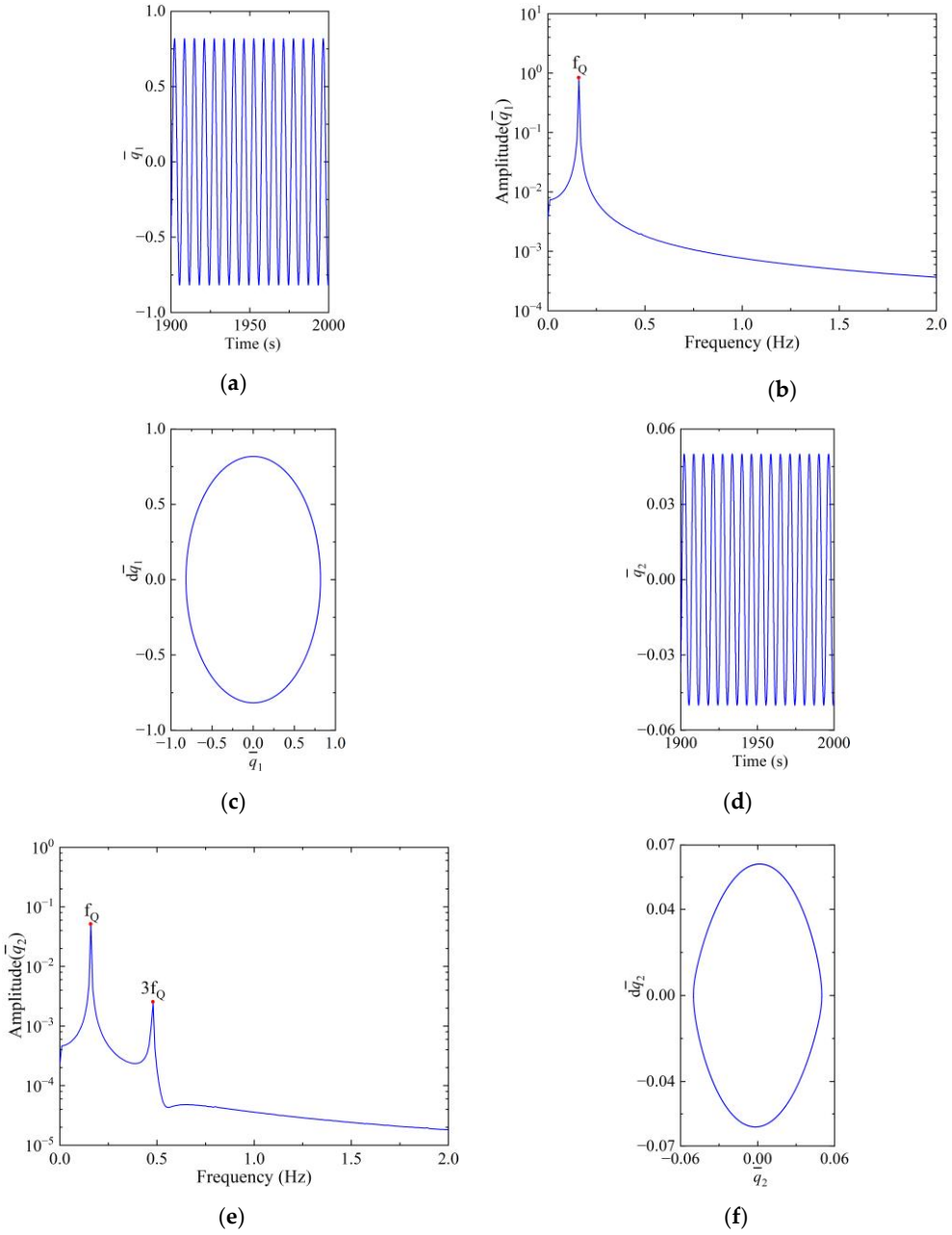

Figure 14. Steady responses of the blade with k_s = 8.191 MN/m. (**a**) Time history, (**b**) frequency spectra and (**c**) phase diagram of $\bar{q}_1$; (**d**) time history, (**e**) frequency spectra and (**f**) phase diagram of $\bar{q}_2$.

4.1.3. The Effect of Rotation Speed

In the following, the contribution of the rotation speed to the blade vibration is studied. The bifurcation of the modal responses is shown in Figure 15, where the range of Ω is from 2000 r/min to 12,000 r/min. This range of speed can also be divided into three stages: $2.0 \times 10^3 \sim \Omega_1$ (stage-I), $\Omega_1 \sim \Omega_2$ (stage-II) and $\Omega_2 \sim 1.2 \times 10^4$ r/min (stage-III), respectively, where $\Omega_1 = 4.46 \times 10^3$ r/min and $\Omega_2 = 8.08 \times 10^3$ r/min.

As shown in Figure 15a, the steady responses of $\bar{q}_1$ remains in a periodic-3 motion for the entire range of Ω. Similar to the case of contact stiffness, $\bar{q}_2$ remains periodic-1 in stages-I and III, while $\bar{q}_2$ is periodic-3 in stage-II, Figure 15b. Moreover, the jumping of the amplitude and the hardening spring can also be observed in stage-II due to the combination resonance.

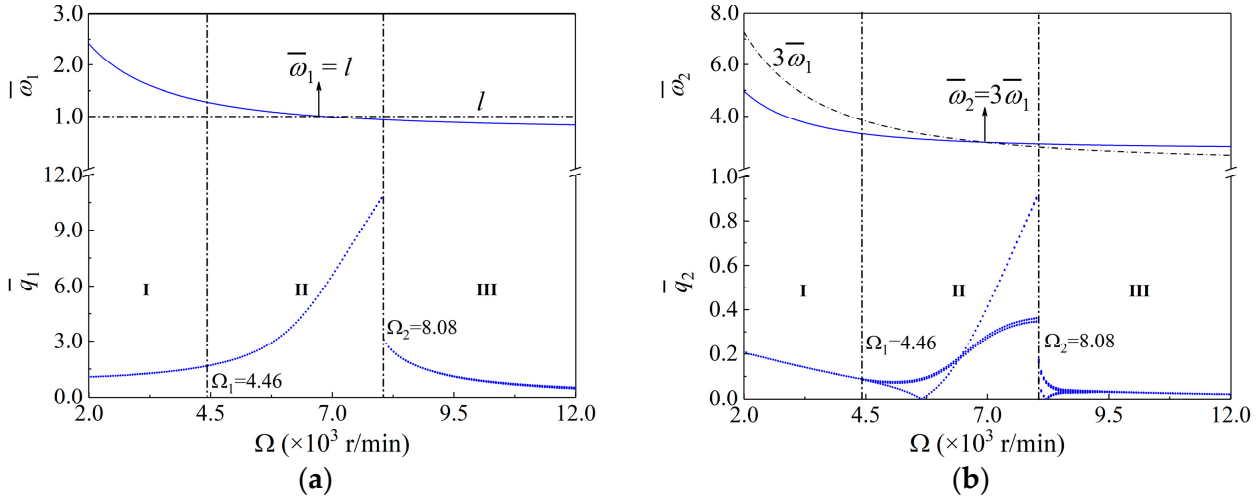

Figure 15. Bifurcation diagram of the blade under variable W. (**a**) $\overline{q}_1$ and (**b**) $\overline{q}_2$.

Next, three values of rotational speed, i.e., 2000 r/min (in stage-I), 7480 r/min (in stage-II) and 11,000 r/min (in stage-III), are chosen to examine the modal responses, Figures 16–18. It is found that the steady first flapwise response is always period-1. However, the second flapwise modal response turns from the period-1 to period-3 motion and then goes back to period-1 with the increasing rotation speed. In addition, exchanges in energy can also be observed in stage-III, a sign of the interaction between modes of the first-order and second-order flapwise motion due to internal resonance.

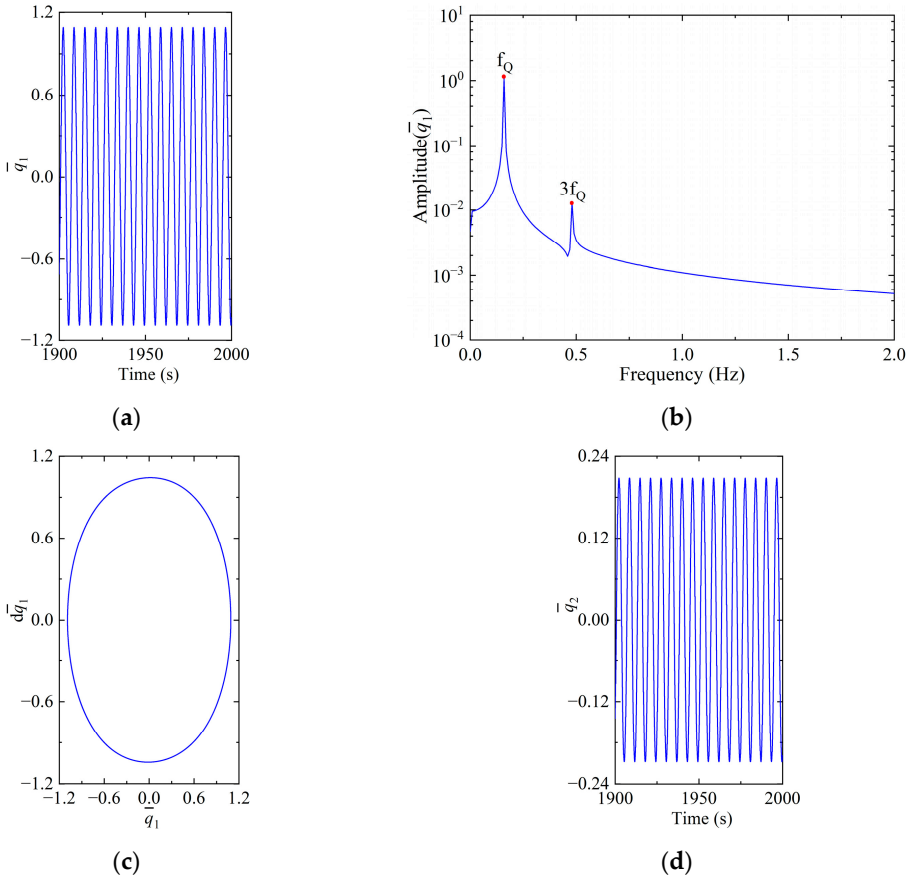

Figure 16. *Cont.*

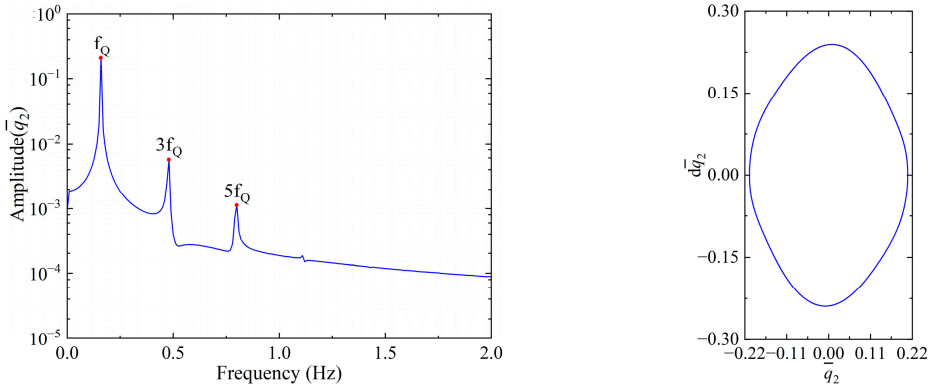

(**e**) (**f**)

Figure 16. Steady responses with Ω = 2000 r/min. (**a**) Time history, (**b**) frequency spectra and (**c**) phase diagram of $\bar{q}_1$; (**d**) time history, (**e**) frequency spectra and (**f**) phase diagram of $\bar{q}_2$.

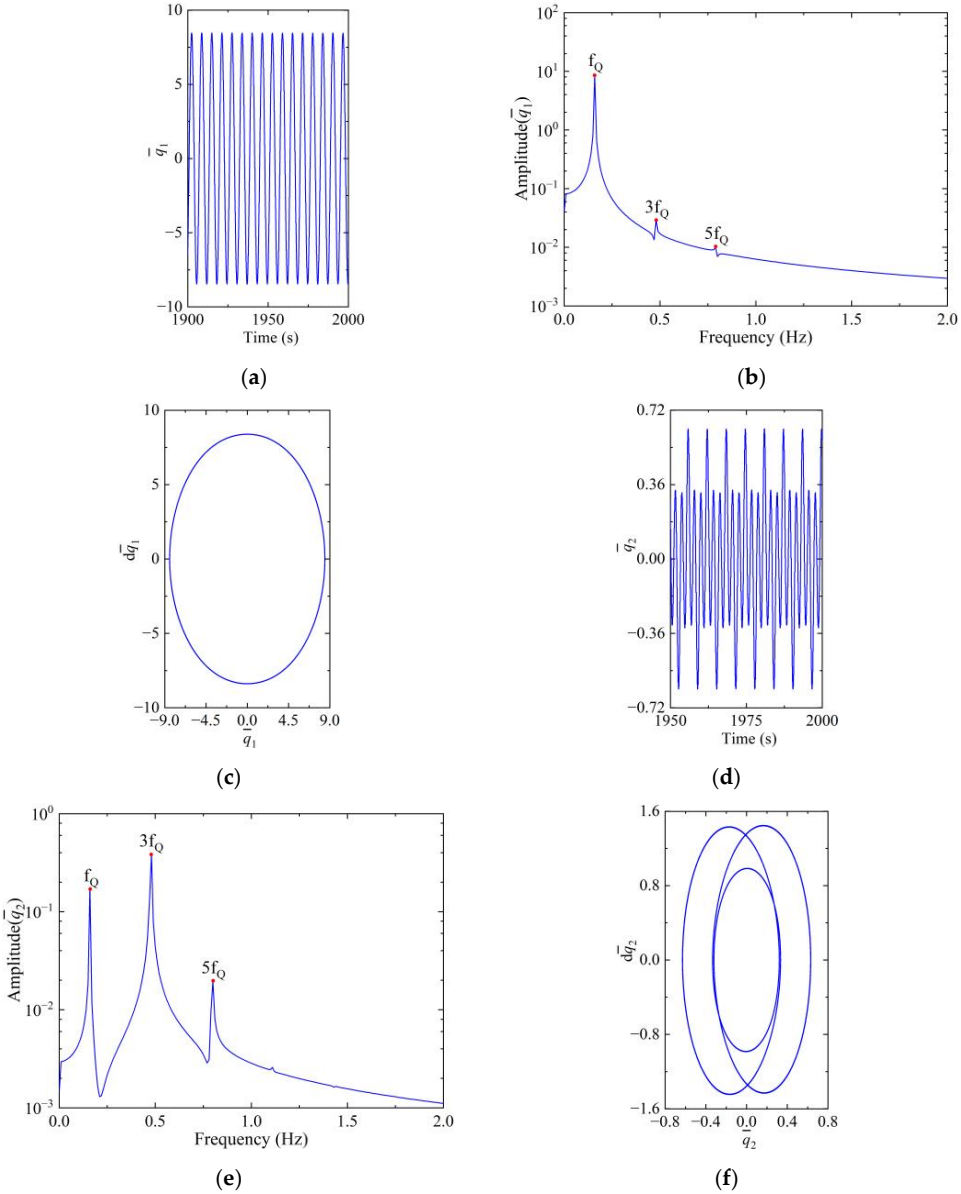

(**a**) (**b**)

(**c**) (**d**)

(**e**) (**f**)

Figure 17. Steady responses with Ω = 7480 r/min. (**a**) Time history, (**b**) frequency spectra and (**c**) phase diagram of $\bar{q}_1$; (**d**) time history, (**e**) frequency spectra and (**f**) phase diagram of $\bar{q}_2$.

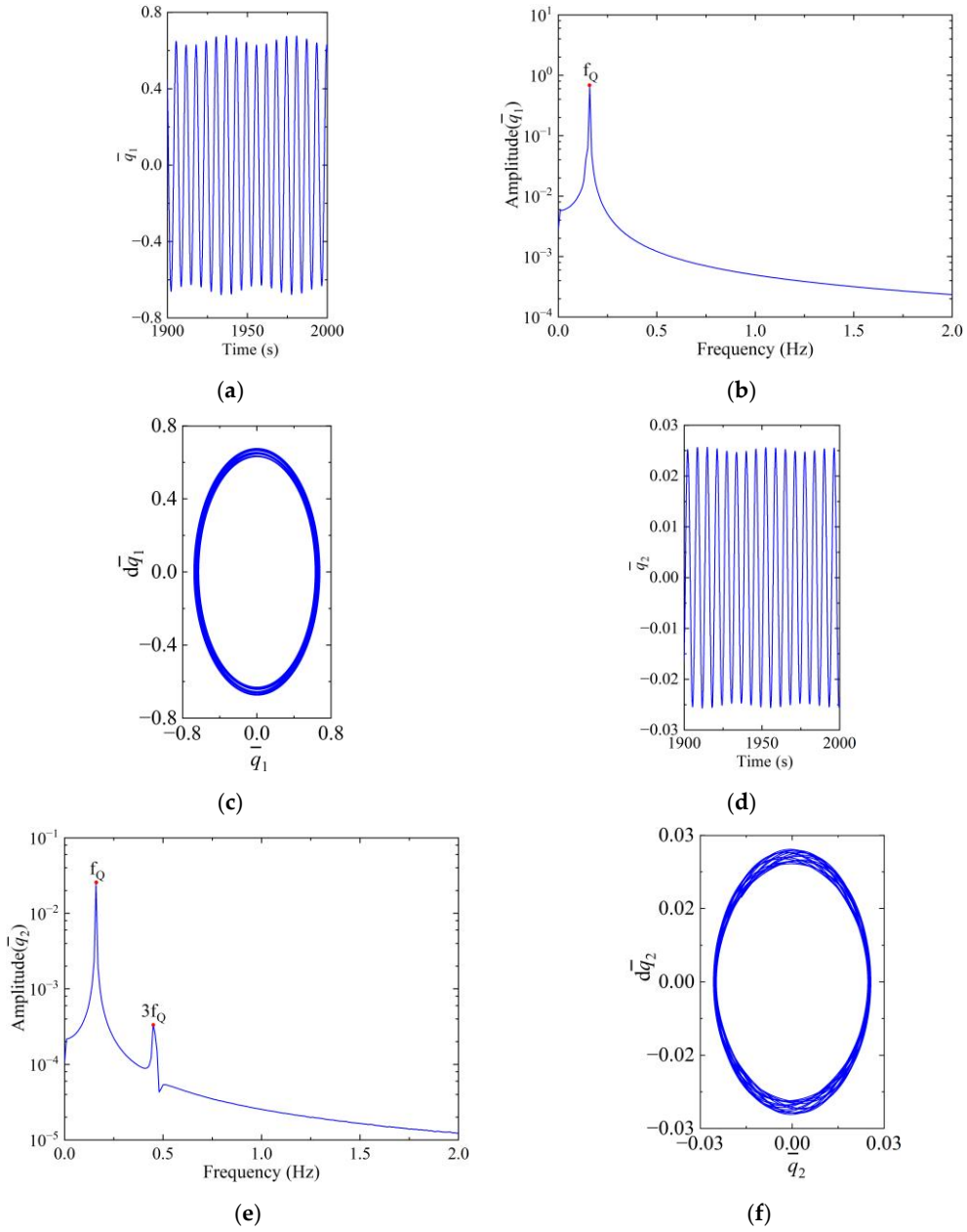

Figure 18. Steady responses with Ω = 11,000 r/min. (**a**) Time history, (**b**) frequency spectra and (**c**) phase diagram of $\bar{q}_1$; (**d**) time history, (**e**) frequency spectra and (**f**) phase diagram of $\bar{q}_2$.

4.2. Parametric Analysis in the Case of Combination Resonance

Based on Section 4.1, both primary and internal resonances can be observed in the steady responses of the first-order and second-order modes in the flapwise motion under variable tilting angle of the shroud, stiffness of normal contact and rotation speed. Also, combination resonance can be identified with the parameters in Table 1. In this section, the parametric influences of detuning and shroud design (δ_s and k_s) are highlighted on the blade response in the case of combination resonance. It is worth noting that the forcing and damping parameters (i.e., $\overline{f}_k$ and $\overline{c}_k$) as well as the geometric nonlinearity coefficients $\overline{g}_{k,j}$ are all related to δ_s and k_s. For convenience, a coefficient of damping is defined for the flapwise modes of interest:

$$\zeta_k = \overline{c}_{k,k}/(2\overline{\omega}_{k,k})$$

Based on Figure 19, for a fixed δ_s, the flapwise damping ratios $\zeta_{1,2}$ rise as k_s increases. Both $\zeta_{1,2}$ decrease with the increasing δ_s when k_s is constant. Further, the effect of δ_s on the

modal dampings of the flapwise motion is noticeably weak compared with that of k_s. In addition, the coefficient of the nondimensional equations in Appendix A shows that $\overline{g}_{k,j}$ ascends as δ_s increases in contrast to $\overline{f}_k$. Both $\overline{g}_{k,j}$ and $\overline{f}_k$ are insensitive to the contact stiffness.

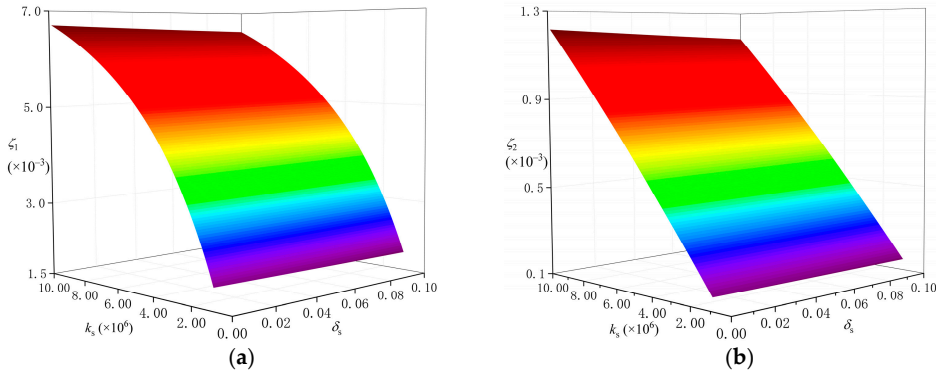

(**a**) (**b**)

Figure 19. Damping ratio of the first and second modes versus δ_s and k_s. (**a**) ζ_1 and (**b**) ζ_2. The colors represent the magnitudes of ζ_1 and ζ_2.

4.2.1. Effect of $\varepsilon\sigma_1$ with Various Contact Stiffness and Gap Dimension

The amplitude–frequency relations of both α_1 and α_2 are presented in Figure 20 using different $\varepsilon\sigma_1$ and constant $k_s = 3.55 \times 10^6$ N/m and $\delta_s = 2 \times 10^{-5}$ m for the case of combination resonance. It is observed that the blade resembles a hardened spring in vibration, which can be attributed to the presence of the $\overline{g}_{k,j}$ terms. Based on Figure 20a, both stable and unstable motions can be identified within different bands of frequency, along with four turning points, i.e., A_1, B_1, C_1 and D_1. The real and imaginary parts of eigenvalues are presented in Figure 21, corresponding to the steady responses depicted in Figure 20.

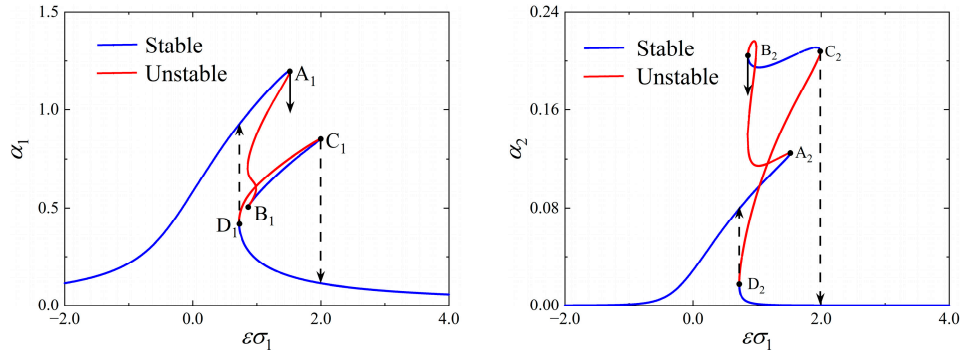

(**a**) (**b**)

Figure 20. Effect of $\varepsilon\sigma_1$ in the case of combination resonance. (**a**) α_1 and (**b**) α_2.

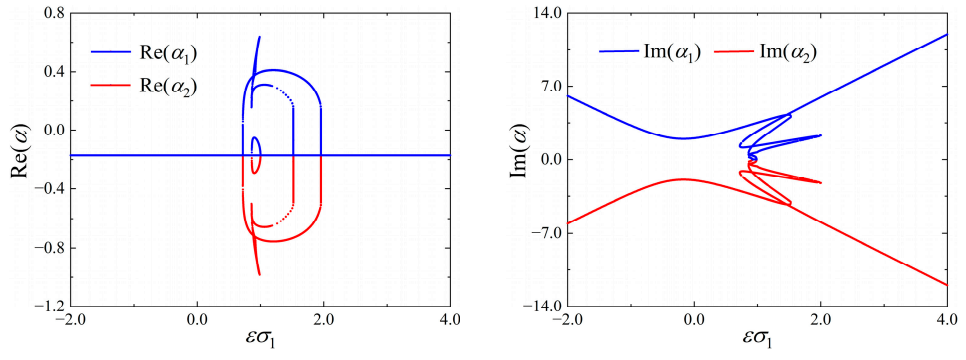

(**a**) (**b**)

Figure 21. Effect of $\varepsilon\sigma_1$ on stability. (**a**) First flapwise mode and (**b**) second flapwise mode.

As far as the fixed points are concerned, the branch left to summit A_1 ($\varepsilon\sigma_1 = 1.52$) are stable focuses of α_1 before the occurrence of primary resonance. The connecting route from A_1 to B_1 ($\varepsilon\sigma_1 = 0.88$) involves identified saddle-typed fixed points that destabilize α_1. The branch between points B_1 and C_1 ($\varepsilon\sigma_1 = 2.00$) has stable focuses at α_1, as opposed to the saddle points represented by the branch from point C_1 to D_1 ($\varepsilon\sigma_1 = 0.72$). Moreover, the branch right of the turning point D_1 returns to a stable focus. As a matter of fact, α_1 jumps downward from A_1 and C_1 once $\varepsilon\sigma_1$ increases to critical values. The upward jumping happens at D_1 as $\varepsilon\sigma_1$ decreases to a certain critical value. However, with the decreasing $\varepsilon\sigma_1$, α_1 will jump at the turning point B_1. The responses either jumps up and flows following the left branch of point A_1 or goes down to the right branch of point D_1.

As for α_2 in the case of combination resonance, a similar phenomenon of hardening can be observed in Figure 20b through three stable regions, two unstable regions and four turning points. Comparing the amplitudes in Figure 20a,b, the branches of response between points B_2 ($\alpha_2 = 0.206$) and C_2 ($\alpha_2 = 0.209$) are greater than that at A_2 ($\alpha_2 = 0.124$), which makes a difference in the direction of jumping at points A_2 ($\varepsilon\sigma_1 = 1.52$) and B_2 ($\varepsilon\sigma_1 = 0.88$); however, α_1 in the branch B_1 ($\alpha_1 = 0.516$) and C_1 ($\alpha_1 = 0.853$) are less than that at A_1 ($\alpha_1 = 1.20$). This confirms the existence of energy exchange between the first and second modes in the flapwise direction.

To demonstrate the effect of contact stiffness, k_s is reduced by half (denoted subsequently by $0.5k_s$) and doubled (by $2k_s$), respectively. The solutions of α_1 and α_2 are presented in Figures 22 and 23, respectively. Unlike the results shown in Figure 20, the decreasing k_s widens the range of frequency corresponding to instability of the vibration and delays the onset frequency for primary resonance. Specifically, the frequency interval for unstable motion expands from (0.88, 1.52) and (0.72, 2.00) to (0.84, 7.05) and (0.83, 10.01), respectively. The larger k_s is able to remove the instability of α_1 and α_2 under the combination resonance alongside the turning points. This is because the damping of the blade rises with the increasing k_s (see Figure 19) and thus refrains the vibration of the blade. When k_s is large enough, the hardening spring-like reaction of the blade at the resonance point can been completely suppressed.

To demonstrate the effect of the shroud gap, the original δ_s is halved (denoted by $0.5\delta_s$) and doubled (by $2\delta_s$), respectively. The solutions of α_1 and α_2 are presented in Figures 24 and 25, accordingly. Similar to the previous finding, the blade vibrates in higher amplitude as δ_s becomes larger, and the onset of primary resonance postpones. In this case, the regions of $\varepsilon\sigma_1$ corresponding to instability expand from (0.88, 1.52) and (0.72, 2.00) to (1.14, 3.05) and (0.93, 3.97) and narrow to (0.60, 0.76) and (0.60, 0.76) in Figure 25 when the gap doubles its original value.

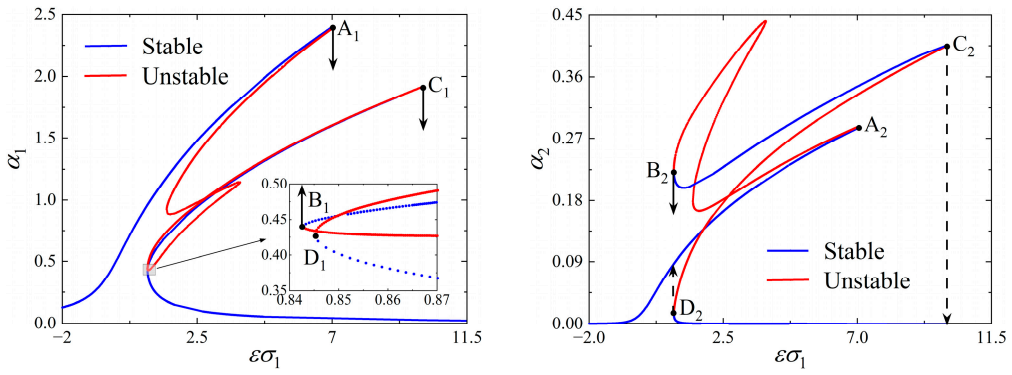

(**a**) (**b**)

Figure 22. Effect of $\varepsilon\sigma_1$ in the case of combination resonance with $0.5k_s$ contact stiffness. (**a**) α_1 and (**b**) α_2.

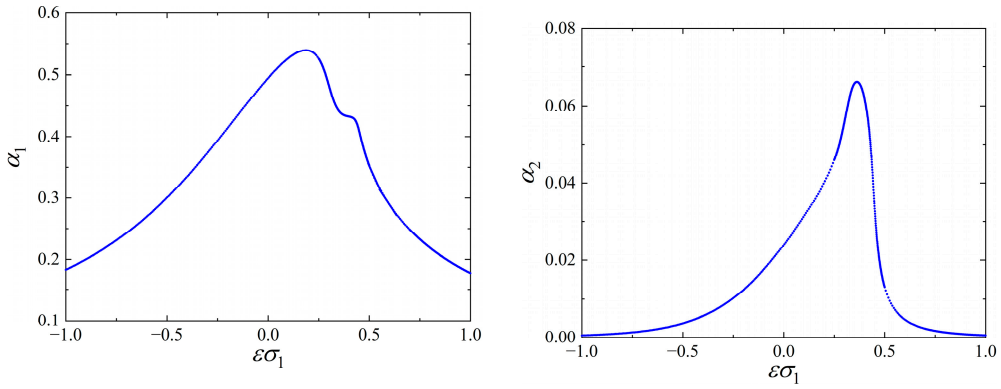

(**a**) (**b**)

Figure 23. Effect of $\varepsilon\sigma_1$ in the case of combination resonance with a $2k_s$ contact stiffness. (**a**) α_1 and (**b**) α_2.

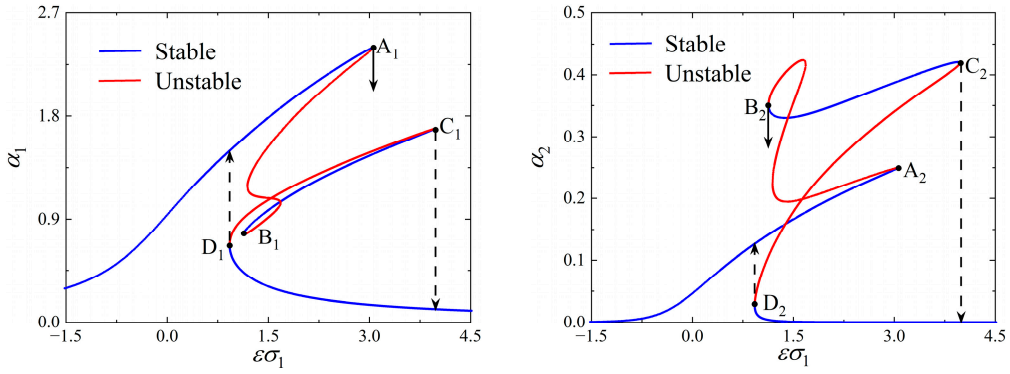

(**a**) (**b**)

Figure 24. Effect of $\varepsilon\sigma_1$ in the case of combination resonance with a $0.5\delta_s$ shroud gap. (**a**) α_1 and (**b**) α_2.

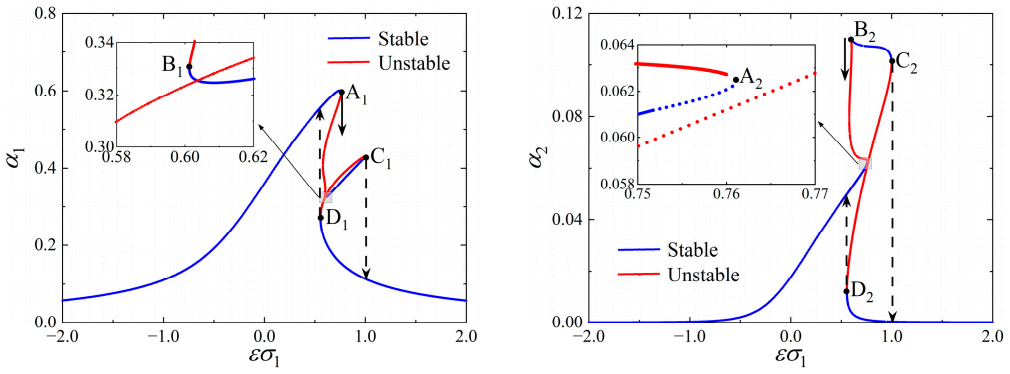

(**a**) (**b**)

Figure 25. Effect of $\varepsilon\sigma_1$ in the case of combination resonance with a $2\delta_s$ shroud gap. (**a**) α_1 and (**b**) α_2.

Nevertheless, the effect of δ_s is noticeably weaker than that of k_s. The rising δ_s influences the level of vibration through changing the aerodynamic force (f_k), damping (ζ_k) and geometric nonlinear terms ($\overline{g}_{k,j}$). It is worth mentioning that changing $\overline{g}_{k,j}$ has negligible contribution to the level of vibration [32,33]. An increasing δ_s has a double effect on the response: it does reduce the blade damping (see Figure 19) and hence increases the amplitudes of α_1 and α_2; on the other hand, it prevents the response by decreasing the aerodynamic force. Comparing Figure 24 with Figure 25, it is found that the level of vibration decreases with the increasing δ_s; thereby, the strengthening of increasing δ_s on the level of vibration overwhelms its weakening.

4.2.2. Effect of $\varepsilon\sigma_2$ with Various Contact Stiffness and Gap Dimension

In this subsection, the contribution of parameter $\varepsilon\sigma_2$ to the steady response of the blade is investigated. Given $k_s = 3.55 \times 10^6$ N/m and $\delta_s = 2.0 \times 10^{-5}$ m, the amplitudes of the first- and second-order modal response of the flapwise motion are plotted in Figure 26. Unlike the previous discussion, the phenomenon of softening spring are discovered due to the geometric nonlinearity associated with $\overline{g}_{k,j}$.

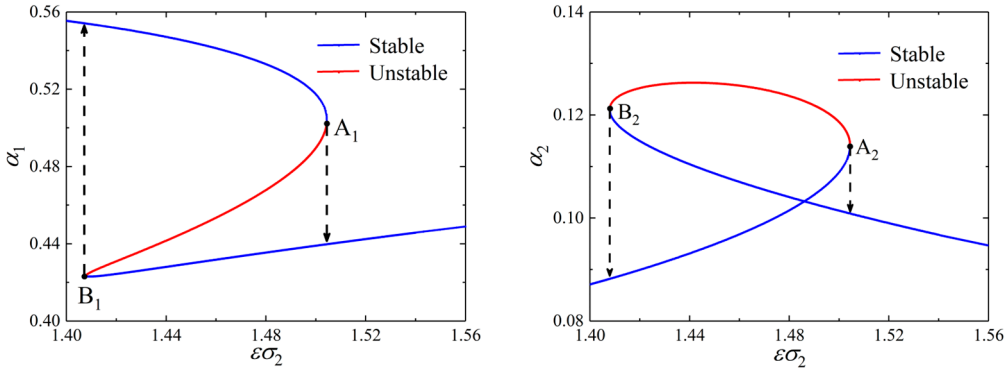

(**a**) (**b**)

Figure 26. Effect of $\varepsilon\sigma_2$ in the case of combination resonance. (**a**) α_1 and (**b**) α_2.

There are two regions of stable motion and one region of unstable motion along with two turning points, i.e., A_1 and B_1, as depicted in Figure 26a. The stability of the steady response is demonstrated through eigenvalue analysis at the fixed points of α_1 and α_2 in Figure 27. In viewing the fixed points, the branch left of point A_1 ($\varepsilon\sigma_2 = 1.504$) is found to be a stable focus of α_1. The connection between A_1 and the lowest point B_1 ($\varepsilon\sigma_2 = 1.408$) corresponds to the saddle points of α_1, demonstrating an unstable motion of the blade. Indeed, α_1 jumps downward from point A_1 once $\varepsilon\sigma_2$ increases to be critical, while an upward jumping is located at point B_1. As shown in Figure 26b, the hardening spring phenomenon can be observed alongside two stable regions and one unstable region. With the increasing $\varepsilon\sigma_2$, α_2 rises in the branch left of the turning point A_2 and drops to the region left of the other turning point B_2, which is opposite to the trend of α_1 in Figure 26a. This suggests that $\varepsilon\sigma_2$ is the key influence on the internal resonance.

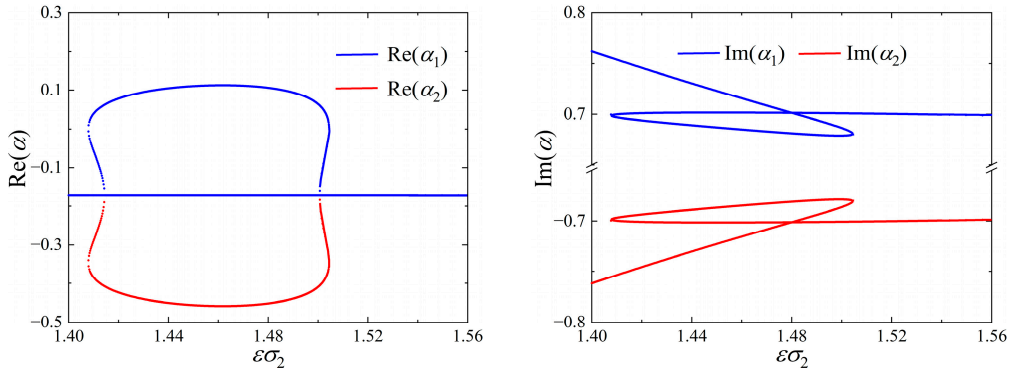

(**a**) (**b**)

Figure 27. Effect of $\varepsilon\sigma_2$ on stability $\alpha_{1,2}$. (**a**) The first and (**b**) second flapwise modes.

The steady responses of the blade vibration versus k_s are presented in Figures 28 and 29 for the combination resonance. As shown in Figure 28, both the level of vibration and the interval of frequency for unstable motion are enlarged. There exists an overlap in the unstable region and the right branch of the turning point B_1. The unstable region expands from $\varepsilon\sigma_2 \in (1.408, 1.504)$ to $(1.423, 1.679)$. Similar to the solutions in Figure 23, the unstable region as well as the turning points can be removed by increasing k_s for the same reason presented in Section 4.2.1.

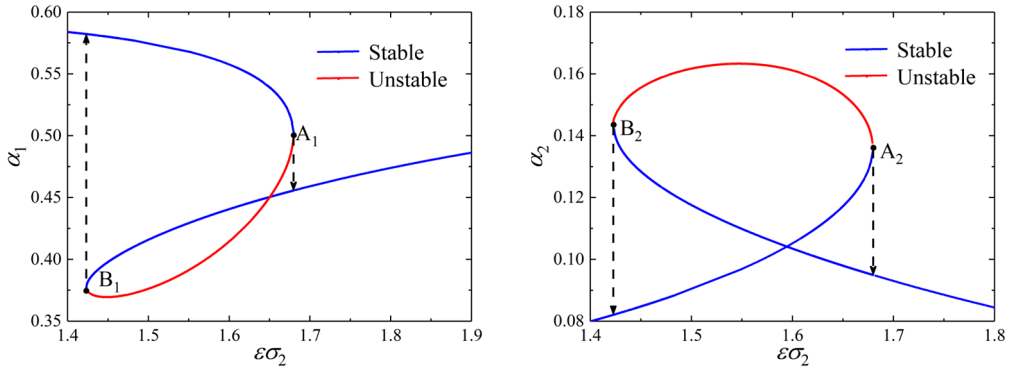

Figure 28. Effect of $\varepsilon\sigma_2$ in the case of combination resonance with $0.5k_s$ contact stiffness. (**a**) α_1 and (**b**) α_2.

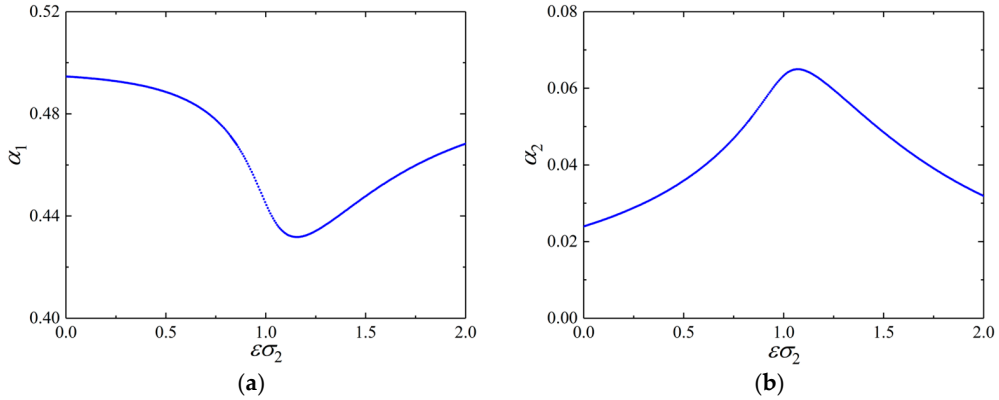

Figure 29. Effect of $\varepsilon\sigma_2$ in the case of combination resonance with $2k_s$ contact stiffness. (**a**) α_1 and (**b**) α_2.

Finally, the steady responses in the situation of combination resonance are presented in Figures 30 and 31 with various shroud gap δ_s. It is found that a decreasing δ_s escalates the vibration level and broadens the interval of instability of motion in the frequency domain. The unstable region now expands from (1.408, 1.504) to (1.783, 1.986) in the frequency domain at a halved δ_s and narrows to (1.097, 1.116) in Figure 31. The effect of k_s on the responses is significantly weaker than that of k_s on $\alpha_{1,2}$. In addition, the overlap in the unstable region and the right branch of the turning point B_1 can also be observed in Figure 30a.

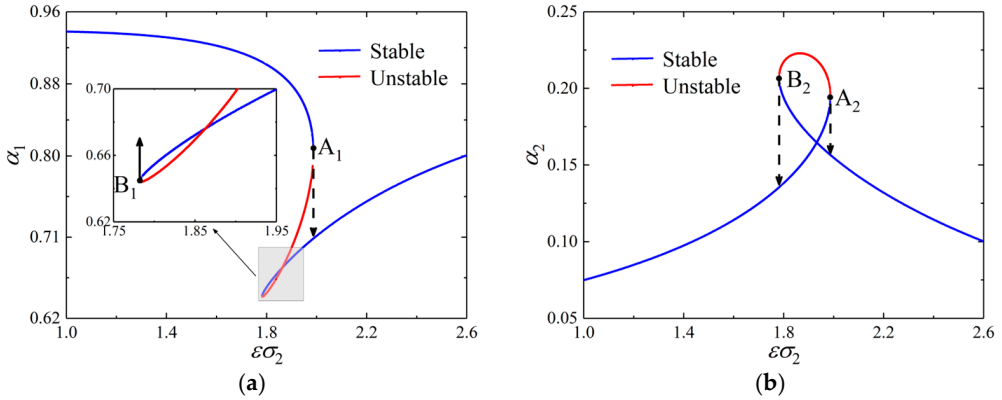

Figure 30. Effect of $\varepsilon\sigma_2$ in the case of combination resonance with a $0.5\delta_s$ shroud gap. (**a**) α_1 and (**b**) α_2.

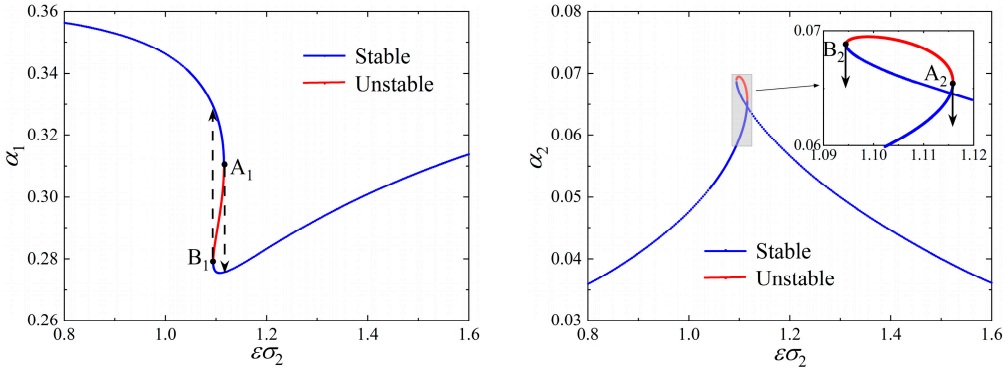

(**a**) (**b**)

Figure 31. Effect of $\varepsilon\sigma_2$ in the case of combination resonance with a $2\delta_s$ shroud gap. (**a**) α_1 and (**b**) α_2.

5. Conclusions

In this paper, the nonlinear dynamics of a flexible turbine blade are investigated considering the contact and friction of shrouds, focusing on the case of combination resonance of flapwise motion induced by a 1:3 internal resonance between the first- and second-order modes and a primary resonance of the first-order mode. The stiffness and damping properties are expressed by linearizing the normal and tangential forces of shrouds using the method of harmonic balance. The steady responses of the blade in the situation of combination resonance are obtained with the multiple-scale method. The contributions of detuning and shroud parameters to the steady responses of the blade in the case combination resonance are analyzed. Several conclusions are drawn as follows:

(1) The combination resonance involving the flapwise modes can be triggered by co-existing internal and primary resonances. Nevertheless, such resonance will not likely occur for separated blades where contact and friction on their shroud interfaces are removed.
(2) Motion of the first-order flapwise mode can change from quasi-periodic to period-1 and then back to quasi-periodic with an increasing tilting angle of shroud. As for the second-order mode, it can change from quasi-periodic to period-3 and finally quasi-periodic.
(3) With increasing contact stiffness and rotation speed, the first-order flapwise motion is period-1, while the second modal response can change between period-1 and period-1.
(4) For primary resonance, the hardening spring behavior of the blade is attributed to geometric nonlinearity in the blade motion. On the other hand, such a nonlinearity can lead to a softening spring behavior of the blade in the scenario of internal resonance.
(5) Less shroud contact stiffness and gap dimension can result in a stronger vibration response, wider region of unstable motion in the frequency domain and delayed onset of combination resonance.

Author Contributions: Conceptualization, H.L. and Y.W.; methodology, G.Y. and Y.W.; validation, H.L. and Y.W.; formal analysis, G.Y.; investigation, H.L. and Y.W.; resources, D.M. and Z.Y.; writing—original draft preparation, H.L. and G.Y.; writing—review and editing, Y.W.; funding acquisition, Y.W. and D.M. All authors have read and agreed to the published version of the manuscript.

Funding: The International Cooperation Fund Project of DBJI, Dalian University of Technology (ICR2109); the Free Exploration Project of the State Key Laboratory of Structural Analysis, Optimization and CAE Software for Industrial Equipment; and the National Science and Technology Major Project (2019-IV-0019-0087).

Data Availability Statement: The data presented in this study are available on request from the corresponding author. The data are not publicly available to protect the information of key design parameters.

Acknowledgments: The authors are grateful to DBJI (the Joint Institute of Dalian University of Technology and Belarus State University) and the State Key Laboratory of Structural Analysis, Optimization and CAE Software for Industrial Equipment for their sponsorships.

Conflicts of Interest: The authors declare no conflicts of interest. The funders had no role in the design of the study; in the collection, analyses, or interpretation of data; in the writing of the manuscript; or in the decision to publish the results. The authors declare that there are not any potential commercial interests.

Appendix A

The coefficients c_k, ω_k, $g_{k,j}$ and f_k of Equation (16) are defined as

$$c_k = \frac{1}{m_k}\left[\int_0^L c_v \gamma_k^{2(v)} dx - \left(c_n \sin\alpha + c_f \cos\alpha\right)\gamma_k^{2(v)}(L)\right] \tag{A1}$$

$$\omega_k^2 = \frac{1}{m_k}\begin{pmatrix} \int_0^L EI\gamma''^{2(v)}_k dx + \int_0^L \int_x^L m_l\Omega^2(e+y)dy\gamma'^{2(v)}_k dx \\ -\int_0^L \Omega^2 m_l \gamma_k^{2(v)} dx_i - \left(\Omega^2 m_s + k_n \sin\alpha + k_f \cos\alpha\right)\gamma_k^{2(v)}(L) \end{pmatrix} \tag{A2}$$

$$g_{k,1} = \frac{1}{m_k}\int_0^L \frac{1}{2} EA\gamma'^{(v)}_k \gamma'^{3(v)}_1 dx \tag{A3}$$

$$g_{k,2} = \frac{1}{m_k}\int_0^L \frac{1}{2} EA\gamma'^{(v)}_k \gamma'^{2(v)}_1 \gamma'^{(v)}_2 dx \tag{A4}$$

$$g_{k,3} = \frac{1}{2m_k}\int_0^L EA\gamma'^{(v)}_k \gamma'^{(v)}_1 \gamma'^{2(v)}_2 dx \tag{A5}$$

$$g_{k,4} = \frac{1}{2m_k}\int_0^L EA\gamma'^{(v)}_k \gamma'^{3(v)}_2 dx \tag{A6}$$

$$f_k = -\frac{1}{m_k} Q_0 \gamma_k^{(v)}(L), \tag{A7}$$

where

$$m_k = \int_0^L m_l \gamma_k^{2(v)} dx + m_s \gamma_k^{2(v)} \tag{A8}$$

The coefficients $\overline{c}_k$, $\overline{\omega}_k$, $\overline{g}_{k,j}$ and $\overline{f}_k$ of Equation (18) are defined as

$$\overline{c}_k = \frac{1}{\Omega m_k}\left[\int_0^L c_v \gamma_k^{2(v)} dx - \left(c_n \sin\alpha + c_f \cos\alpha\right)\gamma_k^{2(v)}(L)\right] \tag{A9}$$

$$\overline{\omega}_k^2 = \frac{1}{\Omega^2 m_k}\begin{pmatrix} \int_0^L EI\gamma''^{2(v)}_k dx + \int_0^L \int_x^L m_l\Omega^2(e+y)dy\gamma'^{2(v)}_k dx \\ -\int_0^L \Omega^2 m_l \gamma_k^{2(v)} dx_i - \left(\Omega^2 m_s + k_n \sin\alpha + k_f \cos\alpha\right)\gamma_k^{2(v)}(L) \end{pmatrix} \tag{A10}$$

$$\overline{g}_{k,1} = \frac{\delta_s^2}{\Omega^2 m_k}\int_0^L \frac{1}{2} EA\gamma'^{(v)}_k \gamma'^{3(v)}_1 dx \tag{A11}$$

$$\overline{g}_{k,2} = \frac{\delta_s^2}{2\Omega^2 m_k}\int_0^L EA\gamma'^{(v)}_k \gamma'^{2(v)}_1 \gamma'^{(v)}_2 dx \tag{A12}$$

$$\overline{g}_{k,3} = \frac{\delta_s^2}{2\Omega^2 m_k}\int_0^L EA\gamma'^{(v)}_k \gamma'^{(v)}_1 \gamma'^{2(v)}_2 dx \tag{A13}$$

$$\overline{g}_{k,4} = \frac{\delta_s^2}{2\Omega^2 m_k}\int_0^L EA\gamma'^{(v)}_k \gamma'^{3(v)}_2 dx \tag{A14}$$

$$\overline{f}_k = -\frac{1}{\delta_s \Omega^2 m_k} Q_0 \gamma_k^{(v)}(L) \tag{A15}$$

The components of $\boldsymbol{J}$ in Equation (32) are defined as

$$J_{1,1} = -\frac{c_{1,1}}{2} - \frac{3g_{1,2}}{4\omega_1}\alpha_1\alpha_2 \sin\gamma_2,\ J_{1,2} = -\frac{3g_{1,2}}{8\omega_1}\alpha_1^2 \sin\gamma_2,\ J_{1,3} = \frac{f_1}{2\omega_1}\sin\gamma_1,\ J_{1,4} = -\frac{3g_{1,2}}{8\omega_1}\alpha_1^2\alpha_2 \cos\gamma_2, \tag{A16}$$

$$J_{2,1} = \frac{3g_{2,1}}{8\omega_2}\alpha_1^2 \sin\gamma_2,\ J_{2,2} = -\frac{c_{2,2}}{2},\ J_{2,3} = 0,\ J_{2,4} = \frac{g_{2,1}}{8\omega_2}\alpha_1^3 \cos\gamma_2 \tag{A17}$$

$$\begin{aligned} J_{3,1} &= -\tfrac{3g_{1,1}\alpha_1}{4\omega_1} - \tfrac{3g_{1,2}\alpha_2}{8\omega_1}\cos\gamma_2 - \tfrac{f_1}{2\omega_1\alpha_1^2}\sin\gamma_1, \\ J_{3,2} &= -\tfrac{3g_{1,3}\alpha_2}{2\omega_1} - \tfrac{3g_{1,2}\alpha_1}{8\omega_1}\cos\gamma_2,\ J_{3,3} = \tfrac{f_1}{2\omega_1\alpha_1}\cos\gamma_1,\ J_{3,4} = \tfrac{3g_{1,2}\alpha_1\alpha_2}{8\omega_1}\sin\gamma_2 \end{aligned} \tag{A18}$$

$$\begin{aligned} J_{4,1} &= -\left(\tfrac{9g_{1,1}}{4\omega_1} - \tfrac{3g_{2,2}}{2\omega_2}\right)\alpha_1 - \left(\tfrac{9g_{1,2}\alpha_2}{8\omega_1} - \tfrac{3g_{2,1}\alpha_1^2}{8\omega_1\alpha_2}\right)\cos\gamma_2 - \tfrac{3f_1}{2\omega_1\alpha_1^2}\sin\gamma_1, \\ J_{4,2} &= -\left(\tfrac{9g_{1,3}}{2\omega_1} - \tfrac{3g_{2,4}}{4\omega_2}\right)\alpha_2 - \left(\tfrac{9g_{1,2}\alpha_1}{8\omega_1} + \tfrac{g_{2,1}\alpha_1^3}{8\omega_1\alpha_2^2}\right)\cos\gamma_2,\ J_{4,3} = \tfrac{3f_1}{2\omega_1\alpha_1}\cos\gamma_1,\ J_{4,4} = \left(\tfrac{9g_{1,2}\alpha_1\alpha_2}{8\omega_1} - \tfrac{g_{2,1}\alpha_1^3}{8\omega_1\alpha_2}\right)\sin\gamma_2 \end{aligned} \tag{A19}$$

Appendix B

An iterative can be applied to solve the amplitude of the steady vibration responses (i.e., B in Equation (2)) before the governing equations in the paper are solved. Let the initial value of B be denoted as B_0. The properties of stiffness and damping can be determined by substituting B_0 into Equations (8), (9), (11) and (12), which represented as $k_{n,0}$, $k_{f,0}$, $c_{n,0}$ and $c_{f,0}$, respectively. Then, the steady responses of Equation (18) along with the transient systems (28)–(31) are solved using $k_{n,0}$, $k_{f,0}$, $c_{n,0}$ and $c_{f,0}$, and the amplitude of the steady response is denoted by B_1. The above process is repeated with B_1 as the initial value until the error between B_i and B_{i-1} is below the preassigned tolerance. At last, B_i is accepted as the amplitude of the desired steady responses.

References

1. Cigeroglu, E. Development of Microslip Friction Models and Forced Response Prediction Methods for Frictionally Constrained Turbine Blades. Ph.D. Thesis, The Ohio State University, Columbus, OH, USA, 2007.
2. Xie, F.; Ma, H.; Cui, C.; Wen, B. Vibration response comparison of twisted shrouded blades using different impact models. *J. Sound Vib.* **2017**, *397*, 171–191. [CrossRef]
3. Ju, D.; Sun, Q. Modeling of a Wind Turbine Rotor Blade System. *J. Vib. Acoust.* **2017**, *139*, 051013. [CrossRef]
4. Chiu, Y.J.; Chen, D.Z.; Yang, C.H. Influence on Coupling Vibration of Rotor System with Grouped Blades due to Mistuned Lacing Wire. *Appl. Mech. Mater.* **2011**, *101–102*, 1119–1125. [CrossRef]
5. Ma, H.; Xie, F.; Nai, H.; Wen, B. Vibration characteristics analysis of rotating shrouded blades with impacts. *J. Sound Vib.* **2016**, *378*, 92–108. [CrossRef]
6. Chatterjee, A.; Kotambkar, M.S. Modal characteristics of turbine blade packets under lacing wire damage induced mistuning. *J. Sound Vib.* **2015**, *343*, 49–70. [CrossRef]
7. Shadmani, M.; Tikani, R.; Ziaei-Rad, S. On using a distributed-parameter model for modal analysis of a mistuned bladed disk rotor and extracting the statistical properties of its in-plane natural frequencies. *J. Sound Vib.* **2019**, *438*, 324–343. [CrossRef]
8. Zhou, X.; Huang, K.; Li, Z. Geometrically nonlinear beam analysis of composite wind turbine blades based on quadrature element method. *Int. J. Non-Linear Mech.* **2018**, *104*, 87–99. [CrossRef]
9. Karimi, A.H.; Shadmani, M. Nonlinear vibration analysis of a beam subjected to a random axial force. *Arch. Appl. Mech.* **2019**, *89*, 385–402. [CrossRef]
10. Griffin, J.H. Friction Damping of Resonant Stresses in Gas Turbine Engine Airfoils. *J. Eng. Power* **1980**, *102*, 329–333. [CrossRef]
11. Menq, C.-H.; Bielak, J.; Griffin, J. The influence of microslip on vibratory response, part I: A new microslip model. *J. Sound Vib.* **1986**, *107*, 279–293. [CrossRef]
12. Iwan, W.D. On a Class of Models for the Yielding Behavior of Continuous and Composite Systems. *J. Appl. Mech.* **1967**, *34*, 612–617. [CrossRef]
13. Yang, B.; Menq, C. Characterization of 3D contact kinematics and prediction of resonant response of structures having 3D frictional constraint. *J. Sound Vib.* **1998**, *217*, 909–925. [CrossRef]
14. Nan, G.; Lou, J.; Song, C.; Tang, M. A New Approach for Solving Rub-Impact Dynamic Characteristics of Shrouded Blades Based on Macroslip Friction Model. *Shock. Vib.* **2020**, *2020*, 8147143. [CrossRef]
15. Brach, R.M. *Mechanical Impact Dynamics: Rigid Body Collisions*; John Wiley & Sons: New York, NY, USA, 1991.
16. He, B.; Ouyang, H.; He, S.; Ren, X.; Mei, Y. Dynamic analysis of integrally shrouded group blades with rubbing and impact. *Nonlinear Dyn.* **2018**, *92*, 2159–2175. [CrossRef]
17. He, S.; Si, K.; He, B.; Yang, Z.; Wang, Y. Rub-Impact Dynamics of Shrouded Blades under Bending-Torsion Coupling Vibration. *Symmetry* **2021**, *13*, 1073. [CrossRef]

18. Mashayekhi, F.; Nobari, A.; Zucca, S. Hybrid reduction of mistuned bladed disks for nonlinear forced response analysis with dry friction. *Int. J. Non-Linear Mech.* **2019**, *116*, 73–84. [CrossRef]
19. She, H.; Li, C.; Tang, Q.; Wen, B. Veering and merging analysis of nonlinear resonance frequencies of an assembly bladed disk system. *J. Sound Vib.* **2021**, *493*, 115818. [CrossRef]
20. Wei, S.-T.; Pierre, C. Localization Phenomena in Mistuned Assemblies with Cyclic Symmetry Part II: Forced Vibrations. *J. Vib. Acoust.* **1988**, *110*, 439–449. [CrossRef]
21. Fang, X.; Tang, J.; Jordan, E.; Murphy, K. Crack induced vibration localization in simplified bladed-disk structures. *J. Sound Vib.* **2006**, *291*, 395–418. [CrossRef]
22. Picou, A.; Capiez-Lernout, E.; Soize, C.; Mbaye, M. Robust dynamic analysis of detuned-mistuned rotating bladed disks with geometric nonlinearities. *Comput. Mech.* **2020**, *65*, 711–730. [CrossRef]
23. Zhao, W.; Zhang, D.; Xie, Y. Vibration analysis of mistuned damped blades with nonlinear friction and contact. *J. Low Freq. Noise Vib. Act. Control.* **2019**, *38*, 1505–1521. [CrossRef]
24. Larsen, J.W.; Nielsen, S.R.K. Nonlinear parametric instability of wind turbine wings. *J. Sound Vib.* **2007**, *299*, 64–82. [CrossRef]
25. Karimi, B.; Moradi, H. Nonlinear kinematics analysis and internal resonance of wind turbine blade with coupled flapwise and edgewise vibration modes. *J. Sound Vib.* **2018**, *435*, 390–408. [CrossRef]
26. Zhang, W.; Liu, G.; Siriguleng, B. Saturation phenomena and nonlinear resonances of rotating pretwisted laminated composite blade under subsonic air flow excitation. *J. Sound Vib.* **2020**, *478*, 115353. [CrossRef]
27. Chu, S.; Cao, D.; Sun, S.; Pan, J.; Wang, L. Impact vibration characteristics of a shrouded blade with asymmetric gaps under wake flow excitations. *Nonlinear Dyn.* **2013**, *72*, 539–554. [CrossRef]
28. Allara, M. A model for the characterization of friction contacts in turbine blades. *J. Sound Vib.* **2009**, *320*, 527–544. [CrossRef]
29. Pai, P.; Rommel, B.; Schulz, M.J. Non-linear vibration absorbers using higher order internal resonances. *J. Sound Vib.* **2000**, *234*, 799–817. [CrossRef]
30. Sayed, M.; Kamel, M. 1:2 and 1:3 internal resonance active absorber for non-linear vibrating system. *Appl. Math. Model.* **2012**, *36*, 310–332. [CrossRef]
31. Eftekhari, M.; Ziaei-Rad, S.; Mahzoon, M. Vibration suppression of a symmetrically cantilever composite beam using internal resonance under chordwise base excitation. *Int. J. Non-Linear Mech.* **2013**, *48*, 86–100. [CrossRef]
32. Li, L.; Li, Y.; Liu, Q.; Lv, H. Flapwise non-linear dynamics of wind turbine blades with both external and internal resonances. *Int. J. Non-linear Mech.* **2014**, *61*, 1–14. [CrossRef]
33. Yuan, G.; Wang, Y. Internal, primary and combination resonances of a wind turbine blade with coupled flapwise and edgewise motions. *J. Sound Vib.* **2021**, *514*, 116439. [CrossRef]
34. She, H.; Li, C. Effects of centrifugal stiffening and spin softening on nonlinear modal characteristics of cyclic blades with impact–friction coupling. *Nonlinear Dyn.* **2022**, *110*, 3229–3254. [CrossRef]
35. Nayfeh, A.H.; Mook, D.T. *Nonlinear Oscillations*; John Wiley & Sons: New York, NY, USA, 1995.